# Gires-Tournois and Michelson-Gires-Tournois Interferometers with Sidewall Bragg Gratings in SOI

by

*Paul Morin*

Department of Electrical & Computer Engineering

McGILL UNIVERSITY

Montreal, Quebec, Canada

August 2016

A thesis submitted to McGill University in partial fulfillment of the requirements of the degree of Master of Engineering.

## Abstract

This thesis investigates the design and measurement of Gires-Tournois Interferometers integrated into silicon photonic circuits. Sidewall-corrugated Bragg gratings are used to make the interferometers and the number of periods is varied to control the reflectances. Additionally, low-reflectance gratings are demonstrated using offset sidewall corrugations to reduce the coupling coefficient of the Bragg gratings. We demonstrate that it is possible to reduce the extinction ratio of our integrated Gires-Tournois Interferometers to ~2 dB by altering the number of grating periods and the sidewall-offset using a configuration that is integratable into silicon photonic circuits. As such, we also demonstrate integration of our devices into a Michelson-Gires-Tournois Interferometer for WDM channel interleaving applications. Our Interleaver devices are designed and measured to operate with 50-to-100 GHz and 100-to-200 GHz channel spacings. Although there are some limitations to using gratings for the interferometer structures, we demonstrate interleavers with extinction ratios up to 15 dB and the desired box-like passbands. Furthermore, by using Bragg gratings, the devices are compact and there is more flexibility in future designs by taking advantage of non-uniform grating profiles.

# Sommaire

Ce mémoire étudie la conception et l'évaluation d'interféromètres de Gires-Tournois intégrés en circuits photoniques sur silicium. Les interféromètres sont fabriqués en réseaux de Bragg ondulés sur les parois latérales, et le nombre de périodes est varié pour contrôler les réflectances. En plus, des réseaux à faible réflectance sont démontrés à l'aide d'ondulations latérales décalées afin de réduire le coefficient de couplage des réseaux Bragg. Nous démontrons qu'il est possible de réduire le taux d'extinction des interféromètres de Gires-Tournois à ~2 dB en modifiant le nombre de périodes des réseaux et le décalage des parois latérales en utilisant une configuration qui est intégrable en circuits photoniques sur silicium. En tant que tel, nous démontrons également l'intégration de nos appareils dans un interféromètre de Michelson-Gires-Tournois pour des applications d'entrelacement de canaux WDM (multiplexage en longueur d'onde). Nos dispositifs entrelaceurs sont conçus et mesurés pour fonctionner à un espacement de canaux de 50 à 100 GHz et 100 à 200 GHz. Bien qu'il existe des limites à l'utilisation des réseaux de Bragg pour les structures de l'interféromètre, nous démontrons des entrelaceurs ayant des taux d'extinction jusqu'à 15 dB et les bandes passantes quasi-rectangulaires souhaitées. En outre, en utilisant des réseaux de Bragg, les dispositifs sont compacts et il y a une flexibilité de design accrue pour des dispositifs futurs en profitant des profils de réseau non-uniforme.

# Acknowledgments

I would like to thank Prof. Lawrence Chen for being an outstanding supervisor and mentor for my Masters degree, I could not do this without his support, discussions, and feedback. Thank you for your speedy email replies, interest in pedagogy, light-hearted nature, and encouraging us to think critically and independently.

Fabrication support was provided via the Natural Sciences and Engineering Research Council of Canada (NSERC) Silicon Electronic-Photonic Integrated Circuits (SiEPIC) Program. The devices were fabricated by Richard Bojko at the University of Washington Nanofabrication Facility, part of the National Science Foundation's National Nanotechnology Infrastructure Network (NNIN). We acknowledge CMC Microsystems, Lumerical Solutions, and Mentor Graphics for support in fabrication, design and CAD tools. I also would like to thank Prof. Lukas Chrostowski for taking me on as a silicon photonics trainee in the SiEPIC program —the workshops, fabrication assistance, and his technical help has driven my research and exposed me to the photonics community in Canada. Thanks to my fellow group members also working on silicon photonics, Behnam Naghdi, Parisa Moslemi, Zefei Wang, Ming Ma, and Dr. Junjia Wang for the help with simulations and measurements.

Finally, I would not be anywhere without the love and support of my parents, family, and my fiancee. Thank you for being there every step of the way and always making an effort to sound interested in my research.

# Contents

# List of Figures

# List of Tables

# Chapter 1

# Introduction

## 1.1 Motivations for Silicon Photonics

Photonic technologies are critical to many systems and devices that permeate countless aspects of our daily lives, including entertainment, medicine, manufacturing, and telecommunications. The latter has had significant impact in shaping our interconnected world, by enabling transmission of massive quantities of data across countries, continents, and oceans, through optical fibres that provide the backbone of the internet.

Compared to electrical systems, photonic technologies offer a number of advantages, such as reduced losses, robustness against electromagnetic interference, and most importantly, significantly higher bandwidth. These advantages have made photonics the technology of choice in long-haul communications because they are able to provide high quality of service and transmission capacity. With a growing global demand for bandwidth year over year and popular adoption of cloud-based services, photonic technologies are being used more frequently in short-haul applications to bring fibre to the home (FTTH) and in datacenters as server interconnects. Unlike long-haul links, datacomm applications demand affordable, and consequentially, mass-producible solutions, with a smaller form-factor that still must outperform electrical systems [1].

Since 1969, the concept of integrated optical interconnects has existed. Much like the integrated circuit, the idea of miniaturizing and connecting multiple photonic components at a monolithic level increases reproducibility of complicated photonic circuits and provide increased isolation from environmental changes, such as temperature [2]. Today, there are a number of platforms that may be used for integrated photonics, such as indium phosphide (InP), silicon nitride (SiN), silica-on-silicon, and silicon-on-insulator (SOI) that have their own advantages and applications. However, since the 1990's, the SOI platform has been predicted to enable optoelectronic integrated circuits (OEICs) and bridge the silicon electronics industry with integrated optics due to its distinct advantages [3]. The first of which is that the high refractive index contrast between silicon and silica ($SiO_2$) enables SOI waveguides (often referred to as silicon nanowires) to have strong optical mode confinement and allows for smaller bend radii than other platforms, leading to a smaller form factor (see Figure 1-1).

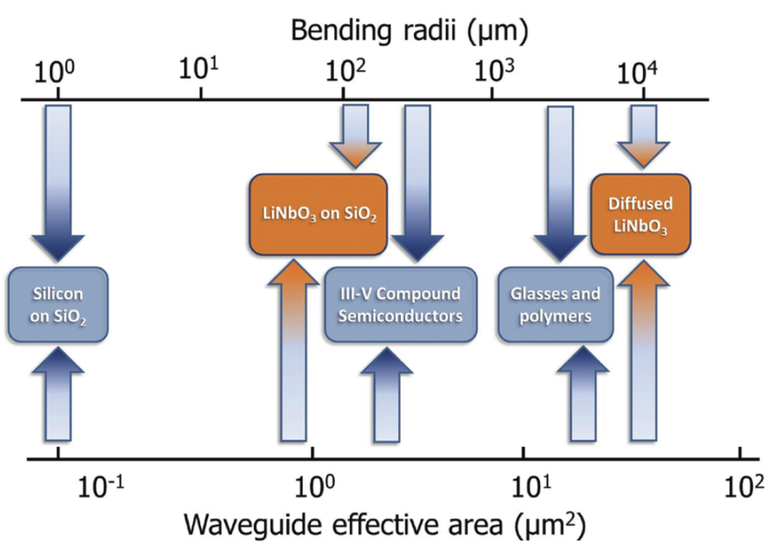


Figure 1-1: Comparison of bend radii and waveguide effective area in integrated photonics platforms [4].

The second major advantage is that the same technology and materials used in the silicon-based microelectronics industry, which has been developed and improved over decades, is used in the SOI platform. Because silicon photonics is compatible with the complementary metal-oxide-semiconductor (CMOS) process used to fabricate microelectronics, and primarily uses abundant materials, the cost of manufacturing photonic integrated circuits (PICs) in SOI is significantly reduced compared to other platforms, making it attractive for datacomm applications. Finally, with the level of integration that is possible with SOI-based PICs, optical interconnects are being developed not only for server-to-server type applications, but applications with higher levels of integration, such as backplane links, module-to-module, chip-to-chip interconnects, and as interposer layers. Photonic integration is key to reducing the I/O bandwidth bottleneck that currently limits performance of high pin-count chips, such as field programmable gate arrays (FPGAs) and application specific integrated circuits (ASICs), and help enable high-performance computers (HPCs) to reach unparalleled capabilities [5].

## 1.2 History of Silicon Photonics

Following the success of electronic integrated circuits and research in fibre optics, integrated photonic circuits were first described in a Bell Systems technical journal in 1969 in which the author envisions photonic integrated circuits consisting of lasers, directional couplers, modulators, crossings, and add/drop filters connected by integrated optical waveguides [2]. Integration of transistors and photonic devices in III-V semiconductor platforms in the 1980's led to the first demonstrations of monolithically integrated photonics [6–8]. Richard Soref's seminal 1987 paper on electro-optic effects in silicon demonstrated that carrier injection or depletion significantly changes the refractive index of silicon, which could be used in phase modulators [9]. In 1993, silicon-based PICs (or "superchips") were proposed by Soref and integrated electronics with many passive photonic components, such as waveguides, couplers and optical filters, as well as active components, such as modulators and detectors, as shown in Figure 1-2 [3].

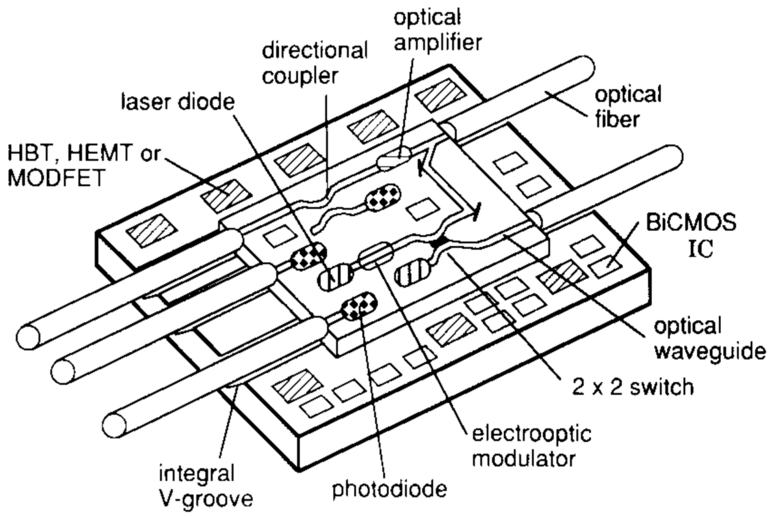


Figure 1-2: "Superchip" consisting of integrated electronics and active photonics on a silicon substrate [3].

PICs using a CMOS process for monolithic photonic and electronic integration have been demonstrated for communication applications by Luxtera and IBM [10, 11]. However, the technology is expensive, limited by the size of the silicon photonic node —which is typically larger than the electronics node — and it does not provide the most efficient use of die area, as such, hybrid integration, where photonic and electronic integrated circuits are on separate dies, holds a greater promise in the new future because it leverages existing technology [12]. Today, several companies, such as Luxtera, Finisar, Oracle Labs, and HP Labs, are working with silicon-based PICs for communication applications using hybrid electronic-photonic integration [13–16].

When hybrid integration is used, the SOI platform is leveraged by standardized processes and design. The process harmonization could enable lower fabrication costs through multi-project wafers (MPW) and compatible devices can be made into libraries and process development kits (PDKs) [12]. Our devices use a 220 nm thick silicon layer for the passive components, which is common to many foundries offering MPW fabrication services [17]. In our devices, components, such as waveguides, vertical grating couplers and Y-branches, are used from existing PDKs and are detailed in chapter 2.

## 1.3 Thesis Objectives and Achievements

The thesis seeks to investigate Gires-Tournois interferometers (GTIs) made from sidewall-corrugated Bragg gratings as a device integratable into silicon-photonic circuits. One such circuit is the Michelson-Gires-Tournois interferometer (MGTI), which can be used as an optical interleaver for WDM applications. We demonstrate GTIs consisting of a waveguide separating two sidewall Bragg gratings, the first of which must have a low ($<$80%) reflectance and the second must be ~100% reflective. Control over the grating reflectance is critical for MGTI interleaver operation, as such two methods are used to reduce the grating reflectance: reducing the number of grating periods and offsetting one grating sidewall by a fraction of the grating period.

We also aim to investigate if these GTIs can be integrated into a simple silicon photonic circuit, the Michelson interferometer, by replacing one or both of the mirrors (gratings) of the Michelson interferometer with a GTI. We demonstrate, for the first time, a grating-based MGTI interleaver on SOI. Although the performance of the MGTI needs to be improved through parameter optimization and phase tuning, the desired box-like passbands of the interleaver spectrum is present.

## 1.4 Publications

The GTIs investigated in chapter 3 have been reported at the following conference presentation:

P. D. Morin and L. R. Chen, "Gires-Tournois Interferometers with Sidewall Bragg Gratings in SOI," *CLEO: Conference on Laser and Electro-Optics*, 5-10 June 2016, San Jose, CA.

## 1.5 Thesis Outline

Chapter 2 introduces silicon photonics and provides background on the fundamentals and components used in our devices. The choice of silicon photonics platform, fabrication, waveguides, waveguide couplers, and vertical grating couplers are discussed. Simulating Bragg gratings using the transfer matrix method is also detailed and sidewall-shifted gratings for controlling the coupling coefficient are introduced.

Chapter 3 introduces the GTI and previous implementations. Our design and simulation results are presented; fabrication and experimental setup are also discussed. Measurement results are presented for GTIs based on uniform and sidewall-shifted gratings and compared with simulations.

Chapter 4 introduces optical interleavers and details the MGTI design. By integrating the GTIs of chapter 3 into a Michelson interferometer silicon photonic circuit, an optical interleaver can be realized. Simulation results of grating-based MGTI interleavers are presented. Four configurations of the design are fabricated and measured. Results are presented and future work is discussed.

Chapter 5 makes conclusions and recommendations for future work.

# Chapter 2

# Silicon Photonics Background

## 2.1 Integrated Photonics Platforms

In microelectronics, the CMOS process has become the workhorse of the industry, yet a ubiquitous integrated photonics platform has yet to be established. If group IV (e.g. silicon, germanium) and III-V (e.g. indium-phosphide, gallium-arsenide) semiconductor platforms for photonics and electronics are heterogeneously integrated on a common substrate, typically silicon, the chip can benefit from the advantages of each platform. The choice of platform in either hetero- or homogeneous photonic-electronic co-integration, is dependent on the application. In the scope of telecommunications, which uses wavelengths around 1.31 μm and 1.55 μm, indium phosphide (InP) is commonly used for high-performance applications, such as long-haul optical links, while silicon photonics is used for short-haul datacomm applications, where cost-effective solutions with high-levels of integration are required.

Our research takes advantage of one of the most commonly used integrated photonics platform, silicon on insulator (SOI), due to its relative maturity and compatibility with existing devices and foundries. A typical SOI wafer consists of a silicon substrate, a buried oxide layer (BOX) and a silicon layer. After the devices are defined, a cladding oxide may be deposited to provide increased robustness and environmental isolation. Furthermore, the SOI platform has a higher level of integration due to a high index contrast between the core and cladding on silicon waveguides. However, the SOI platform exhibits higher losses at telecom wavelengths; has an indirect band-gap, meaning carrier injection is difficult and light-sources in silicon are not very feasible; and at higher optical intensities, two-photon absorption occurs, which hinders non-linear applications [4]. For long-haul applications, indium phosphide (InP) has been the platform of choice due to the ability to integrate lasers and other active devices into photonic integrated circuits. Some of the highest degree of photonic integration has been demonstrated in InP, such as the 500 Gb/s transmitter PIC shown in Figure 2-1 which integrates over 400 functions [18]. Silicon photonics remains relevant due to its compatibility with the CMOS process and cheap materials, which akin to integrated electronics, is poised to enable cost-effective solutions. Because the SOI platform has a high index contrast, it often requires features with sizes on the order of only 10s or 100s of nanometers, which is limited by the fabrication process.

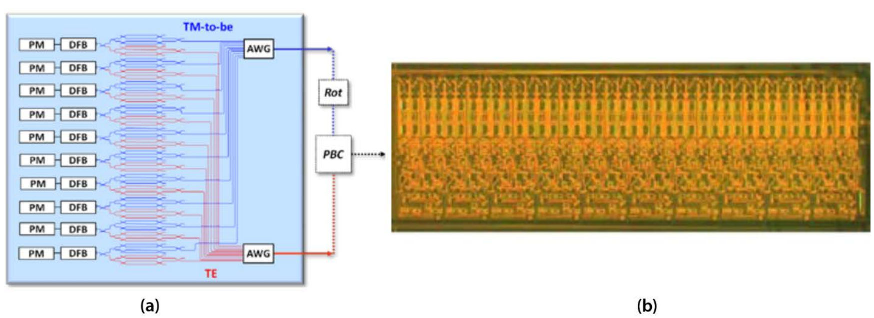


Figure 2-1: (a) Schematic of an integrated 500 Gb/s transmitter PIC on the InP platform consisting of power monitors (PM), distributed feedback lasers (DFB), nested Mach-Zehnder modulators (MZM), arrayed waveguide (AWG) multiplexers, a polarization rotator (Rot), and a polarization beam combiner (PBC); (b) micrograph of chip showing active block (PMs, DFBs, and MZMs) [18].

## 2.2 Fabrication

When integrated circuits (ICs) are fabricated, features are defined using photolithography, in which light passes through a mask to expose patterns on a light-sensitive resist, before etching the features into the desired layer. However, the minimum feature size is limited by the wavelength of the incident light, as such, the microelectronics industry has moved from mercury lamps, with wavelengths around 400 nm, to excimer lasers (248 nm for KrF, 193 nm for ArF lasers) for deep UV lithography (DUV). Use of resolution enhancing techniques, such as immersion lithography, in which the light travels through a series of lenses followed by a liquid medium with a larger refractive index than air, has pushed 193 nm lithography to enable CMOS microelectronics on the 16 nm technology nodes [19]. However, in MPW silicon photonics fabrication, there is an approximate 5 times increase in cost per $mm^2$ between 0.18 μm and 90 nm CMOS technology nodes and the chip area of advanced technology nodes is not efficiently used because photonic devices are typically much larger than integrated electronics [12]. Table 2.1 compares three commercially available MPW fabrication services for silicon photonics R&D using DUV lithography. While silicon photonics fabrication using the CMOS technology platform offers a mature process with high reproducibility and efficient scale-up to higher volumes, it is limited to feature sizes on the order of a few hundred nanometers, as such many silicon photonic chips are prototyped using electron-beam lithography.

In electron-beam lithography (EBL), the pattern is written directly into an electron-sensitive resist using a focused electron beam, making it a maskless process. Electrons have wavelengths determined by their momentum which can be estimated from the acceleration voltage in an electron-beam system (ignoring relativistic effects) by $\lambda \approx \sqrt{1.5/(\text{acceleration voltage})}$ [20]. Thus for an EBL system with a 100 kV acceleration voltage, an electron wavelength of ~3.8 pm is present, making EBL an extremely precise tool for nanofabrication; typical EBL resolutions are on the order of 10s of nanometers

Table 2.1: Comparison of MPW foundries for active silicon photonics [12].

| | IME/OpSIS | IMEC/ePIXfab | CEA-LETI/ ePIXfab |
|---|---|---|---|
| **Passives** | Si passives with 60nm, 130 nm and 220 nm etch depths | Si passives with 70nm, 130 nm and 220 nm etch depths, extra poly-Si layer | Si passives with 70nm, 130 nm and 220 nm etch depths |
| **Photodetector** | Ge vertical *pin* | Ge vertical *pin* | Ge lateral *pin* |
| **Modulator** | Si MZ, Si ring | Si MZ, Si ring | Si MZ |
| **Heater**[1] | doped Si | doped Si | --- |
| **Couplers** | Vertical and edge | Vertical | Vertical |
| **Wavelength Supported**[2] | 1310 and 1550 nm | 1310 and 1550 nm | 1550 nm |
| **CAD Tools** | Mentor Graphics/ Lumerical | Mentor Graphics/ IPKISS/Phoenix | Mentor Graphics/ Phoenix |
| **Packaging** | PLC Connections/ Chiral | Tyndall National Institute | Tyndall National Institute |
| **Pricing**[3] | \$1800 - 2200 USD/mm$^2$ | \$1330 – 1550 EUR/mm$^2$ | \$1400 – 2500 EUR/mm$^2$ |

or less. Due to the direct-write nature of EBL, throughput is much lower than DUV fabrication and it is typically used in silicon photonics for research prototypes and mask production for DUV systems [21].

## 2.3 Waveguides

Optical waveguides are an essential component in any optical system and provide means of confining light. The same principles are used for optical transmission in everything from fibre optic cables thousands of kilometres long to intra-chip connections in integrated photonics that are only micrometers in length. Waveguides operate on the principle of total internal reflection (TIR), in which a critical angle, $\theta_c$ , exists for light propagating from a medium with a higher refractive index, $n_1$ , to a lower index medium, $n_2$ . Beyond $\theta_c$ , the light is reflected at the interface, as shown in Figure 2-2. In optical waveguides, a higher index medium, known as the core, is surrounded by lower index media, know as cladding; light is confined to the core by TIR. Optical confinement can be in one dimension, forming a planar waveguide, or in two dimensions, forming a channel waveguide. The refractive index profile in waveguides can be a step between the core and cladding, as in the SOI platform, providing a strong index contrast between silicon and silica, or a graded index profile, such as in multimode optical fibres in order to reduce modal dispersion [22].

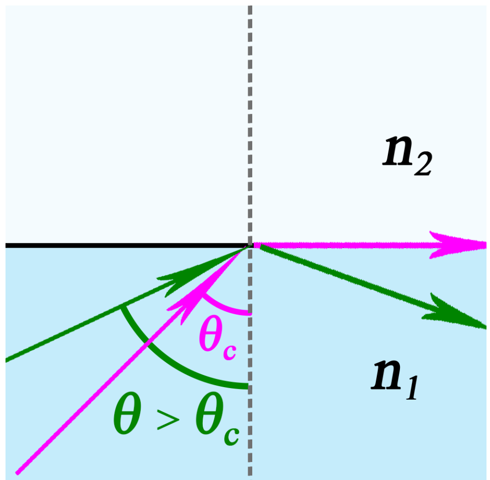


Figure 2-2: Total internal reflection occurs when incident angle is greater than the critical angle.

In silicon photonics, channel waveguides are used with step index profiles and benefit from the high index contrast between silica and silicon. Figure 2-3 shows common channel waveguide configurations that may be used in integrated photonics. Because the waveguides we use in our devices have a cladding oxide layer, they are most similar to Figure 2-3 (a). A cross-section of the waveguides used in our devices is show in Figure 2-4 (a). Light is guided in the 220 nm-thick silicon core ($n_1 \approx 3.5$) and confinement is provided by a 2 μm-thick buried oxide layer and a 2 μm-thick cladding oxide layer ($n_1 \approx 1.45$).

Figure 2-4 (b) shows the relative mode intensity distribution in a buried channel waveguide for the fundamental transverse-electric (TE)-like mode at a wavelength of 1550 nm, in which there is very little electric field in the direction of propagation. We use the term "TE-like" for rectangular waveguides to differentiate it from a true TE mode in a planar waveguide. The results are simulated using a commercially-available mode-

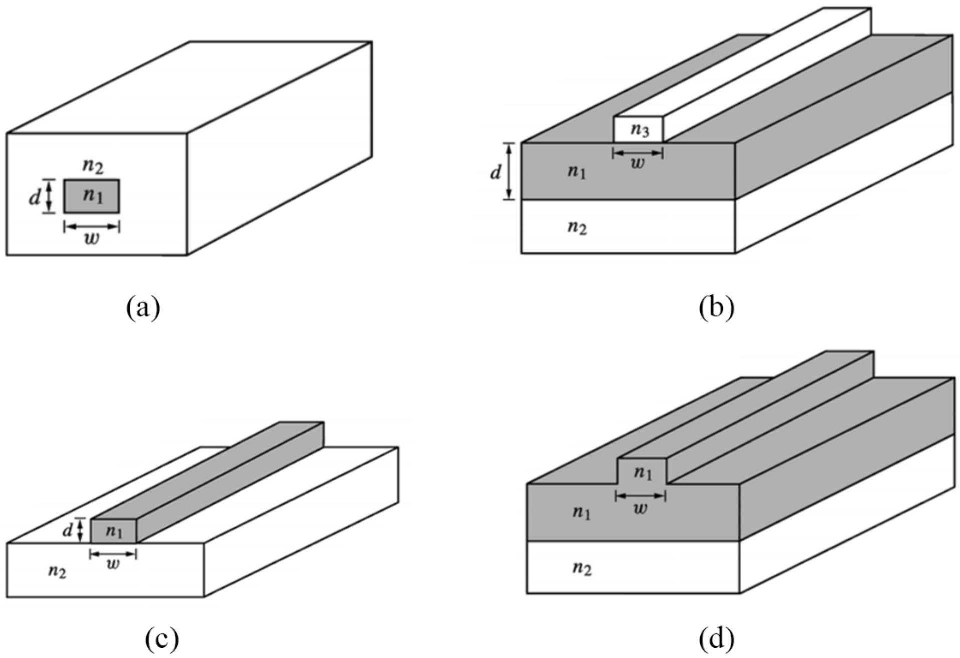


Figure 2-3: Common types of channel waveguides; (a) buried channel waveguide, (b) strip-loaded waveguide, (c) strip waveguide, (d) rib waveguide. $n_1$ is the core, $n_2$ is the cladding and $n_1 > n_2$ [23].

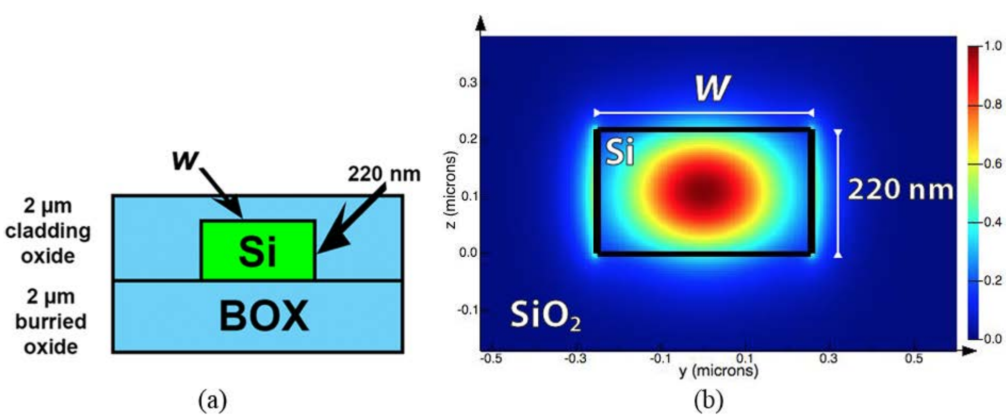


Figure 2-4: (a) Schematic of waveguide cross section used in our devices. (b) intensity profile for the first TE-like mode simulated using Lumerical MODE at a wavelength of 1550 nm.

solver (Lumerical MODE) on a waveguide with the same cross-section as the ones used in our devices. When discussing the refractive index in waveguides, it is important to understand that the bulk (or material) indices of silicon and silica are related to the phase velocities of the electromagnetic waves and are wavelength and temperature dependent, with values of ~3.47 and ~1.45 at 1550 nm and room temperature (297 K), respectively [24,25]. It is noted that in Figure 2-4 (b), while most of the mode is confined to the center of the core, some of it penetrates into the cladding layers, which changes the refractive index of the waveguide, as such, the effective index for the waveguide, $n_{eff}$, is related to the propagation constant, $\beta$, of the waveguide by $n_{eff} = c\beta/\omega$, where $\omega$ is the angular frequency, and $c$ is the speed of light in a vacuum. The effective index in a waveguide has contributions from both the bulk indices of the core and cladding materials and the dimensions and geometry of the waveguide. In fact, the effective index must lie somewhere between the material indices of silicon and silica (i.e. $n_2 < n_{eff} < n_1$). Furthermore, like the bulk refractive index, $n_{eff}$ is dependent on temperature and wavelength. In devices designed for WDM applications on the telecomm C-band (1530 nm to 1565 nm in wavelength), such as the ones we investigate, it is important to understand the dispersive properties of the effective index. Figure 2-5 (a) shows the effective index as a function of a wavelength for the aforementioned 220 nm-thick SOI buried channel waveguides at two widths, 460 nm (red) and 500 nm (blue), as calculated using Lumerical MODE. As the wavelength is increased, a decrease in the effective index is observed, as is the case in the bulk indices of silicon and silica. As the width is decreased, more of the mode is contained in the lower-index cladding layers and the effective index is decreased. While the refractive index is related to the phase velocity of the electromagnetic wave, the group index, $n_g$, is related to the group velocity and can be defined in terms of wavelength by . Because WDM optical devices operate over a range of wavelengths, the group index is an important design parameter. Figure 2-5 (b) shows the group index of 220 nm-thick SOI waveguides with widths of 500 nm and 460 nm.

The waveguide thickness and width are chosen to support only the fundamental TE-like mode. If the waveguide dimensions are large enough they support higher-order modes; the modes travel at different speeds, have their own group indices, and will arrive at different times —a phenomenon known as intermodal dispersion (see Figure

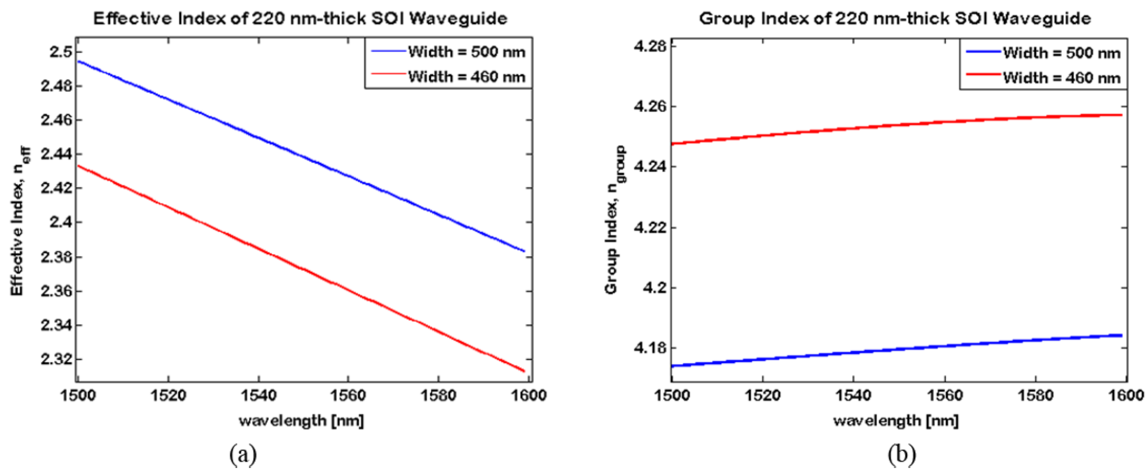


Figure 2-5: Dispersive (a) effective indices and (b) group indicies of 220 nm-thick buried channel SOI waveguides simulated using Lumerical mode at two waveguide widths (500 nm and 460 nm).

2-6). Furthermore, not all components can support higher-order modes, resulting in mode-dependent losses in optical circuits. For this reason, we want to use single-mode waveguides in our devices that are 500 nm wide and 220 nm thick.

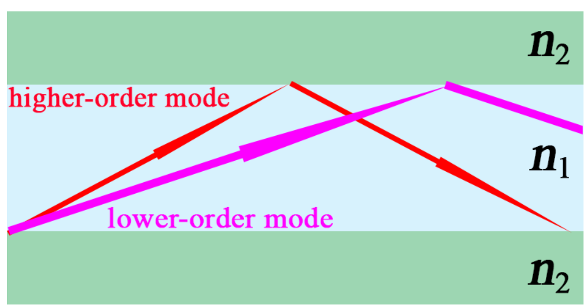


Figure 2-6: Concept of modal dispersion; the higher-order mode has to travel further than the lower-order mode and results in a delayed arrival time.

Whether or not modes are supported is determined by the cutoff conditions of a waveguide. For a waveguide with a fixed height, geometry, and materials, the supported modes are dependent on the waveguide width and wavelength. Figure 2-7 shows the phase space for the two lowest TE and TM modes. In order to support only one TE or TM mode, a waveguide width of 500 nm is selected. By being near, but below, the $TE_2$

cutoff, the waveguide has single-mode operation with lower losses than for a narrower waveguide.

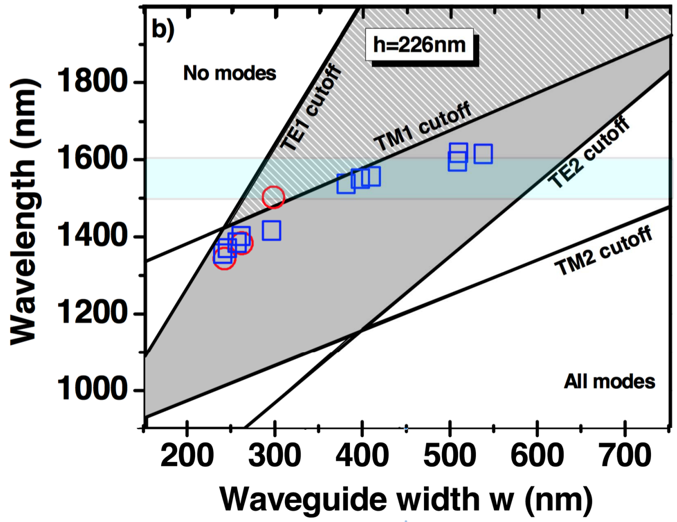


Figure 2-7: Supported modes in a 226 nm-thick rectangular silicon waveguide on a 1 µm-thick silica layer without an oxide cladding [26]. The blue strip is added to show wavelengths that are near or in the telecom C-band.

Optical attenuation in waveguides is critical performance parameter that may determine the application of a waveguide. Optical fibers must have extremely low losses in order to maximize the distance between optical amplifiers or repeaters; a typical single-mode optical fibre, Corning SMF-28 ultra, has a propagation loss $\leqslant$ 0.18 dB/km [27]. Part of what allows silica optical fibres, such as SMF-28, to have such low attenuation is that the refractive index in the core and cladding is very similar. In silicon nanowires, such as the ones detailed in this thesis, strong optical confinement is essential to optical integration but the high index contrast between silicon and silica introduces high losses. Silicon photonic waveguides, 220 nm-thick, typically have losses on the order of 3.5 dB/cm [28, 29]. There are different attenuation mechanisms in optical waveguides: absorption from waveguide materials (intrinsic) and impurities (extrinsic); waveguide imperfections, such as scattering from small fluctuations in refractive index; and scattering from sidewall roughness. The dominant loss in silicon waveguides is due to sidewall roughness from the etching process. In Figure 2-4 (b), some of the mode profile exists outside the waveguide core and penetrates into the cladding, for this reason, sidewall roughness at the interface is detrimental to waveguide performance. Furthermore, when the waveguides are bent, the waveguide mode is pushed to the outside edge of the bend and more losses are present as more of the mode is scattered by the sidewall roughness. Figure 2-8 shows an SEM image of silicon nanowire waveguides —on an image at this scale, sidewall roughness becomes highly visible [30].

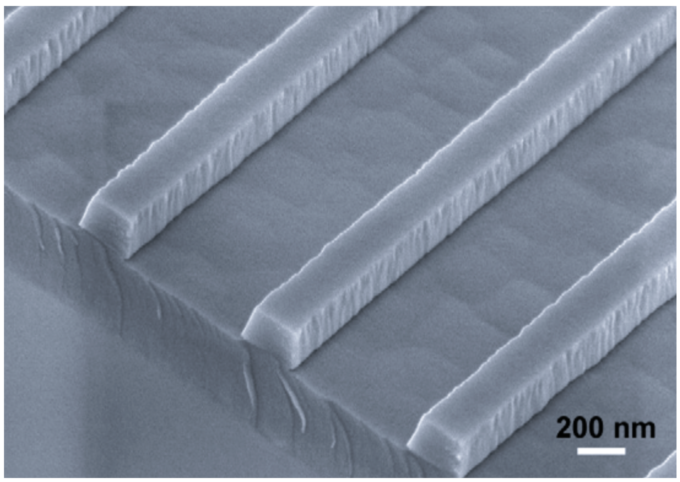


Figure 2-8: SEM micrograph of rectangular silicon waveguides showing sidewall roughness [30]

## 2.4 Waveguide Couplers

Couplers serve the role of splitting or directing light into multiple paths and are a key component of PICs. For example, in interferometric circuits, light is split into two paths and recombined to produce an interference pattern —a task that can only be accomplished using optical couplers. There are a number of types of couplers, such as co-directional couplers, in which a forward propagating mode is coupled into a parallel waveguide, which may be used to split light with into two paths with a specified coupling ratio or, as shown in Figure 2-9, function as an optical switch. Contra-directional couplers use a strong perturbation on the propagation constant, such as a periodic corrugation known as a Bragg grating, to couple light from a forward propagating mode to a backward propagating mode in the same or a parallel waveguide. The theory behind Bragg gratings is detailed in section 2.6.

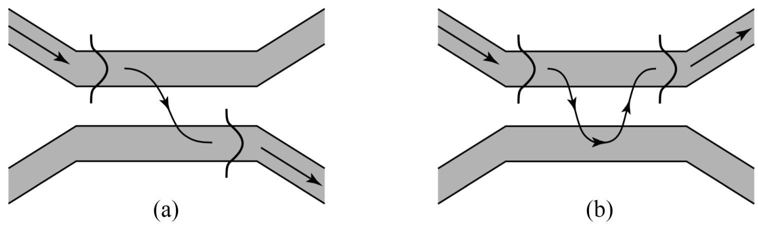


Figure 2-9: Co-directional coupler acting as a 2×2 optical switch in (a) cross state and (b) bar state [23].

While directional couplers offer design flexibility and can be modelled analytically using coupled-mode theory, they exhibit a strong wavelength and temperature dependence. Y-branches offer a compact and low loss alternative to directional couplers for 50/50 power splitting, but unlike other couplers, Y-branches are only able to be configured as a three-port device, i.e. a combiner or a splitter. The Y-branches used in our devices are from Zhang *et al* and have a footprint of only 1.2 µm 2 µm and are reported to have an insertion loss of ~0.3 dB [31]. The electric field distribution, as simulated using finite-difference time-domain (FDTD) method, is shown in Figure 2-10. Due to their compact size, Y-branches are particularly useful for designing test structures for integrated photonic devices that operate in reflection. In bulk and fibre configurations, an optical circulator is used to separate input and reflected light, but there is no compatible magneto-optic material to enable this application on-chip [32]. Figure 2-11 compares an optical circulator-based configuration with a Y-branch for measuring devices in reflection. However, since the Y-branch splits the optical power 50/50 out of each port, an additional 3 dB loss is present at the reflection output port.

Multimode interference (MMI) devices provide means to create integrated N×M couplers. MMI couplers are based on the self-imaging principle in a multimode waveguide in which for a given width, there are periodic intervals where the input field profile is

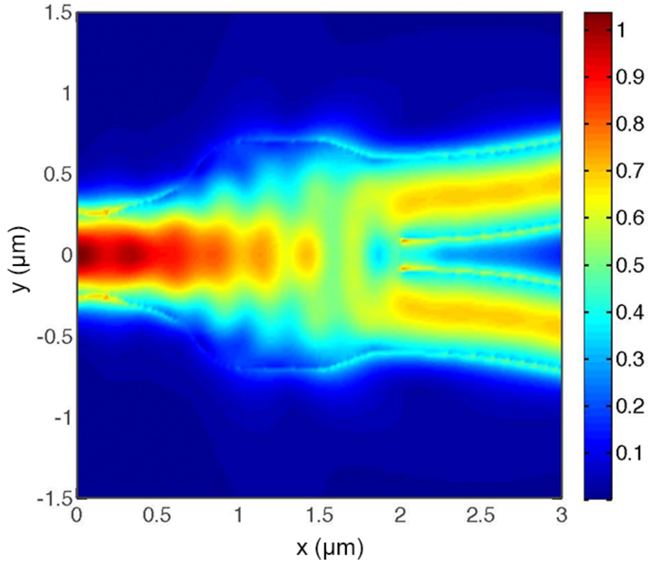


Figure 2-10: FDTD simulation of compact Y-branch showing electric field distribution in a 50/50 power splitting application [31].

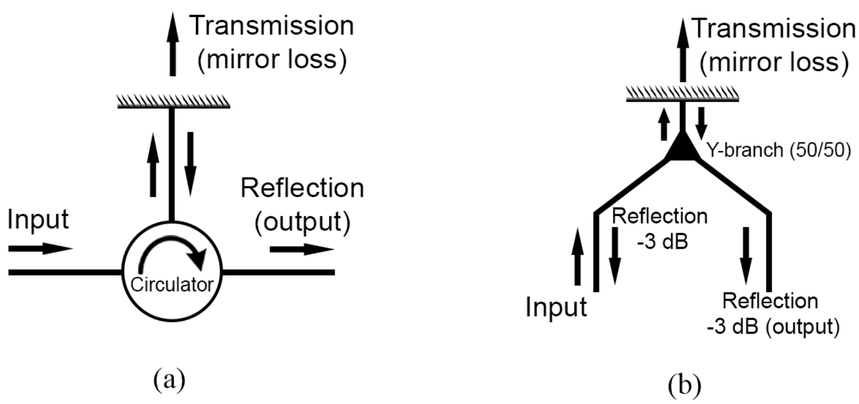


Figure 2-11: Configurations for reflection-based devices: (a) optical circulator and (b) Y-Branch splitter.

reproduced in single or multiple copies [33]. In interferometer applications where 50/50 splitting is desired, an MMI coupler can be designed such that the input electric field profile is duplicated at the outputs. A schematic of the 2×2 MMI couplers used in the devices in this thesis is shown in Figure 2-12. The core of the MMI coupler is a multimode waveguide that is 6 µm-wide and 128 µm -long, such that a coupling ratio of 50:50 is achieved. The MMI coupler has input and output waveguides tapered from 500 nm to 1.5 µm over a length of 20 µm in order to convert the mode field diameter to the multimode waveguide and has 20 μm-long S-bends in order to separate the arms and thereby avoid coupling.

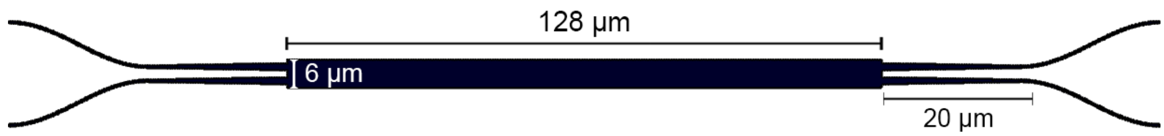


Figure 2-12: Schematic of a 2×2 MMI coupler used in our devices with multimode waveguide and taper dimensions labelled

## 2.5 Vertical Grating Couplers

Perhaps the most performance hindering metric of any silicon PIC is the insertion loss (IL) present when coupling to or from optical fibers to silicon waveguides. This is attributed to the difference in the mode field diameter (MFD) between an optical fiber (MFD ~10 μm) and the waveguide (MFD < 1μm); optical power contained in the larger mode is not effectively coupled into the waveguide and a coupling structure is required to reduce the MFD to the appropriate size. Furthermore, waveguide structures are highly birefringent and the state of polarization (SOP) in optical fibers is random which means that the IL may be increased if polarization compensation is not used. The two most common methods for coupling to PICs are edge coupling with tapered optical fibers and vertical coupling with grating structures.

Edge coupling requires a gradual change in refractive index from that of the silicon waveguide structure that of the silica optical fiber. An example of a low loss structure for edge coupling at telecomm wavelengths is a 500 nm wide and 220 nm thick silicon nanowire waveguide that is slowly tapered down to 80 nm. A 3.5 μm-thick oxide layer is then deposited and partially etched to form a rib waveguide in silica with a MFD similar to the lensed optical fiber, as shown in Figure 2-13. With this configuration, in-plane coupling can be achieved with losses ~1 dB over the entire datacomm and telecomm bands. However, the coupling edge must be polished, lensed fibers are not cheap, and testing is difficult because coupling can only occur at device edges and requires a high level of alignment precision [34].

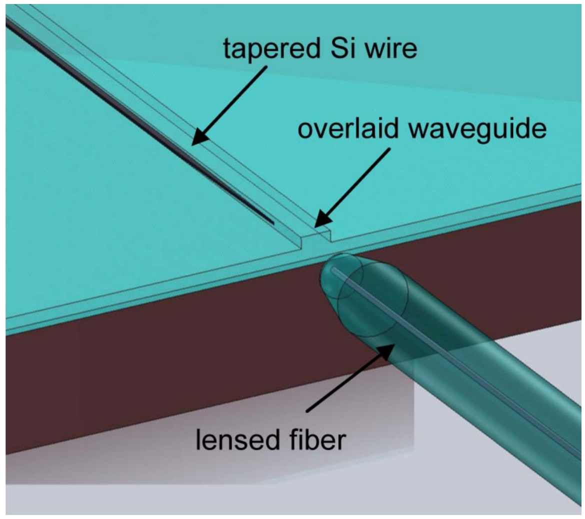


Figure 2-13: Typical edge coupling configuration. Coupling losses are reduced by "squeezing" the mode of the fibre to fit the silicon waveguide using a lens and a tapered waveguide [34].

Conversely, vertical grating couplers (VGC) provide out-of-plane coupling that allows for inputs and outputs to be placed virtually anywhere on the PIC which enables more complex designs and significantly reduces testing costs through wafer-scale automated measurement. However, this is at the cost of bandwidth sensitivity, acceptance of only one polarization, and higher IL than edge couplers, mainly due to back-reflections. VGCs have an adiabatic taper from the fiber core diameter to the waveguide width with the grating placed at the wide end of the taper that couples the light from the fiber to the guided mode in silicon waveguide. When coupling to PICs, it often makes more sense to have vertical grating couplers [35]. In our device we utilize a fully-etched sub-wavelength VGC design from Y. Wang et al that has a reported insertion loss of ~4 dB as shown in Figure 2-14 (b) [36]. However due to the small feature size, this grating coupler is only able to be used in our devices if they are fabricated by Electron-beam writing.

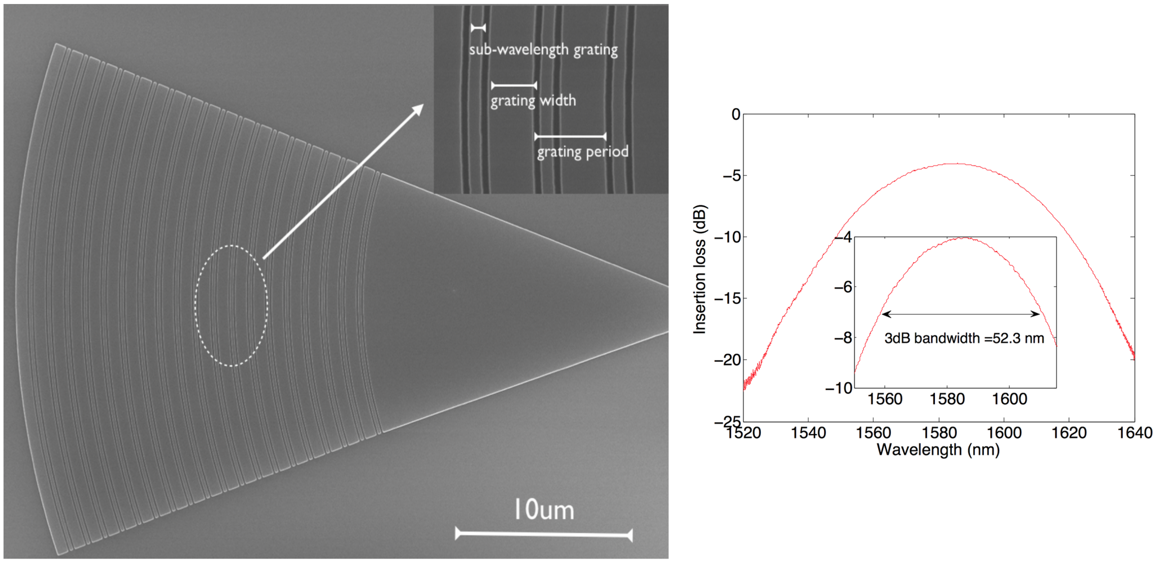


(a) (b)

Figure 2-14: (a) SEM image and (b) insertion loss of a sub-wavelength VGC from Y. Wang et al used in our E-beam photonic devices [36].

## 2.6 Waveguide Bragg Gratings

Grating waveguide couplers utilize a periodic refractive index modulation to couple light from forward to backward propagating modes. The modulation may be achieved through changes in the refractive index of the material, or through structural corrugations in the waveguide. Bragg gratings are a resonant structure that interfere constructively at some wavelengths and destructively at others, effectively making the structure a wavelength-dependent mirror. In optical fibres, exposure to UV light causes an irreversible change in the fibre index and a periodic exposure can be used to make fibre Bragg gratings (FBGs) which have found many applications in communications and sensing [37].

Bragg gratings integrated into SOI waveguides have been demonstrated since 2001 [38]. As shown in Figure 2-15, index modulation in integrated photonics can be achieved through (a) ion implantation [39, 40]; (b) periodic, full- or partial-etching of the top of the waveguide [38, 41]; and (c) through etching sidewall corrugations [42]. Sidewall corrugation is the method of choice for integrated Bragg gratings due to the simplicity (single-etch) in the fabrication process and control over the corrugation depth. Many devices have been demonstrated using sidewall Bragg gratings, such as bandpass filters, chirped microwave pulse generators, and optical add-drop multiplexers (OADM) [43–45].

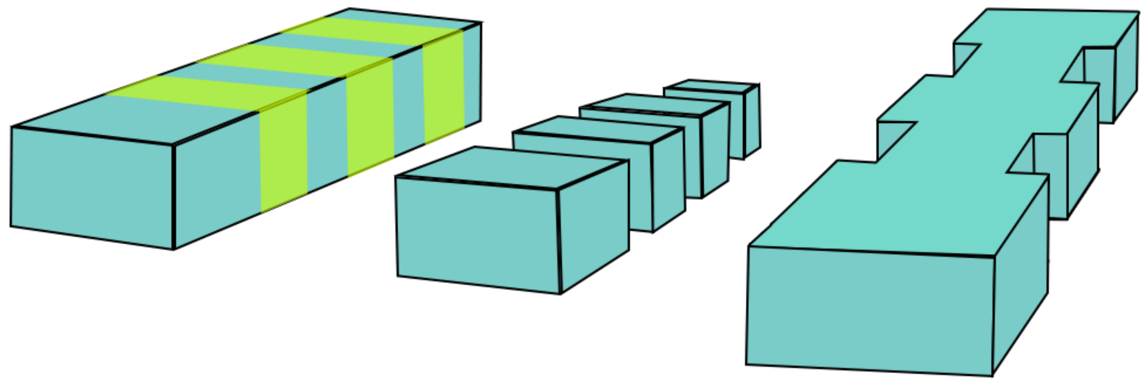


Figure 2-15: Types of integrated waveguide gratings: (a) localized material index change from ion implantation; (b) top full-etched gratings —can also be partially etched in order to reduce the index contrast between the grating segments; (c) sidewall Bragg gratings, such as the ones detailed in this thesis.

A waveguide Bragg grating is a contra-directional coupler that operates in a single waveguide and couples a forward propagating mode with $\beta_a$ to a backward propagating mode with $\beta_b$; the difference in the propagation constants is:

$$\Delta\beta = \beta_b - \beta_a \tag{2.1}$$

In the case of a Bragg grating, at the central wavelength of the grating response, we must have the forward and backward propagating modes matched in phase, as such, the propagation constant, $\beta$, must satisfy:

$$\beta \equiv \beta_a = -\beta_b \tag{2.2}$$

Following [23], the perturbation has a wavenumber, $K = 2\pi/\Lambda$ where $\Lambda$ is the grating period that must satisfy the Bragg condition for phase matching, defined as:

$$\beta_B = q\frac{K}{2} \tag{2.3}$$

where $q$ is an integer representing the order of Bragg grating; in our devices, we use a first-order grating ($q = 1$). The wavelength at the Bragg grating reflection peak, known as the Bragg wavelength, $\lambda_B$ is determined from the Bragg propagation constant:

$$\lambda_B = 2\pi\frac{\overline{n_{eff}}}{\beta_B} \tag{2.4}$$

where $\overline{n_{eff}}$ is the average waveguide effective index of the grating. The grating pitch required for a given wavelength is:

$$\Lambda = q\frac{\lambda_B}{2\overline{n_{eff}}} \tag{2.5}$$

Graphically, the Bragg wavelength, $\lambda_B$, for the gratings used in our devices is determined using equation 2.5 and is shown below in Figure 2-16 The grating is designed to have a 20 nm corrugation depth and as waveguides have with widths of 500 and 460 nm, simulated in Lumerical MODE as per Figure 2-5 (a); the grating period, $\Lambda$, is 320.5 nm. Using the average effective index of 500 and 460 nm waveguides, the phase matching condition for the selected grating pitch is shown as the intersection of the average effective index and . The Bragg wavelength is determined to be 1545.8 nm —a value chosen because it lies within the telecom C-band. It is noted that a longer grating period increases the Bragg wavelength, e.g. a grating period of 321.5 nm has a Bragg wavelength of 1548.6 nm.

The 500 nm-wide waveguide has a higher effective index ($n_{eff_h} = 2.443$) than the thinner waveguide ($n_{eff_l} = 2.377$) and the index difference at the Bragg wavelength is:

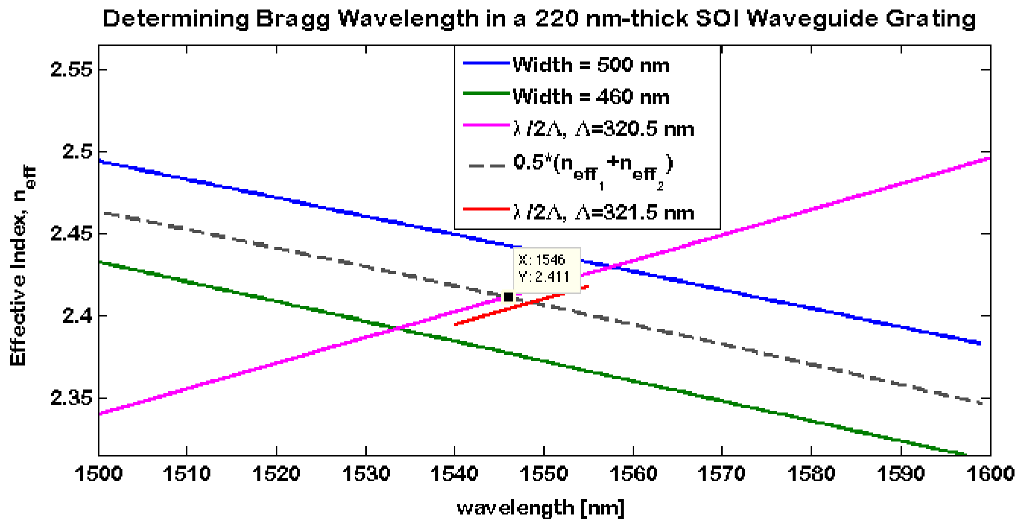


Figure 2-16: The Bragg wavelength is determined graphically to be 1545.8 nm using the average effective index and a Bragg period of 320.5 nm; if a period of 321.5 nm is used, the Bragg wavelength is 1548.6 nm. Phase matching occurs at the intersection, as such, the wavelength at the intersection corresponds to the center wavelength of Bragg grating reflection band.

$\Delta n_{eff} = n_{eff_h} - n_{eff_l} = 2.443 - 2.377 = 0.066$. The complex reflection coefficient of the Bragg grating is calculated using the following equation [23]:

$$r = \frac{i\kappa_{ba} \sinh \alpha_c l}{\alpha_c \cosh \alpha_c l + i\delta \sinh \alpha_c l} \tag{2.6}$$

where $l$ is the length of the grating coupler and

$$\alpha_c = \sqrt{\kappa_{ab}\kappa_{ba} - \delta^2} \tag{2.7}$$

The phase detuning is given by

$$\delta = -\beta + q\frac{K}{2} \tag{2.8}$$

The reflection coefficient is maximized when $\delta = 0$ which occurs at $\beta(\lambda_B) = \beta_B$. As the wavelength is shifted away from the Bragg wavelength, the reflection coefficient changes accordingly.

Figure 2-17 shows a schematic of the sidewall-etched Bragg gratings we use in our devices. The perturbation is a periodic change in the effective index, $\Delta n_{eff}$, between the wide and narrow segments of the grating. A 20 nm corrugation depth is selected which translates to 460 nm-wide narrow segments of the Bragg grating.

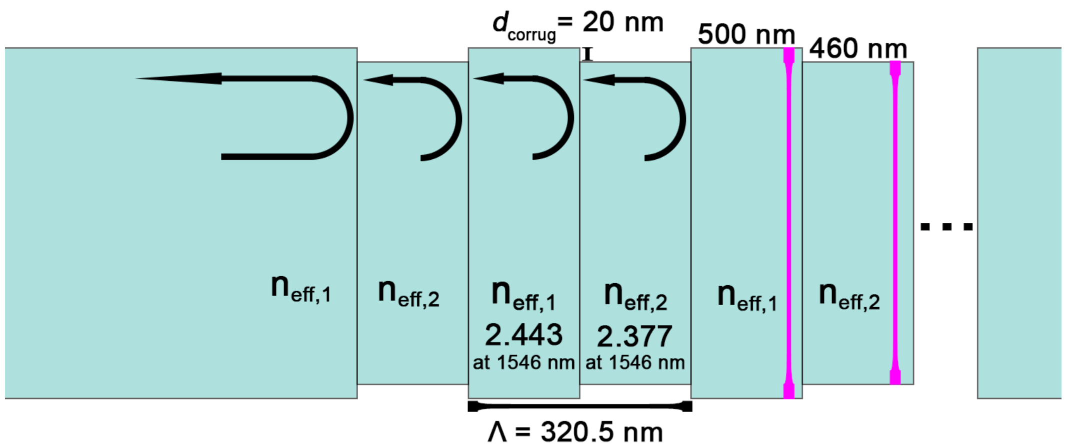


Figure 2-17: Schematic of sidewall Bragg gratings used in our devices.

The reflection coefficient at each interface in the grating is given by the Fresnel equation for normal incidence:

$$r_{\text{norm}} = \frac{\Delta n_{eff}}{n_{eff_1} + n_{eff_2}} \tag{2.9}$$

Recalling that $\overline{n_{eff}}$ is the average effective index of the grating, if the grating has a duty cycle of 0.5, then $n_{eff} = 0.5(n_{eff_1} + n_{eff_2})$ and $r_{\text{norm}} \sim \Delta n_{eff}/2\overline{n_{eff}}$. The coupling coefficient is a measure of the complex reflection per unit length and each grating period experiences two reflections, the coupling coefficient can be estimated as:

$$\kappa \approx \frac{\Delta n_{eff}}{\overline{n_{eff}}} \cdot \frac{1}{\Lambda} = \frac{2\Delta n_{eff}}{\lambda_B} \tag{2.10}$$

Using the values previously determined for our grating, the coupling coefficient at the Bragg wavelength, ~1546 nm, is estimated:

$$\kappa|_{\lambda_B} = \frac{2\Delta n_{eff}|_{\lambda_B}}{\lambda_B} = \frac{2 \cdot 0.066}{1.546\mu m} = 0.0854\mu m^{-1} \tag{2.11}$$

The peak reflectance of a Bragg grating occurs when phased-matched, such that $\delta = 0$, making $\alpha_c = \kappa$ from equations 2.6, and 2.7 can be expressed as:

$$R_{\text{peak}} = |i \tanh \alpha_c l|^2 = \tanh^2 \kappa l \tag{2.12}$$

The peak grating reflectance can also be expressed in terms of number of grating periods, $N = l/\Lambda$, as:

$$R_{\text{peak}} = \tanh^2 (\kappa|_{\lambda_B} N\Lambda) \tag{2.13}$$

Using a value of $N = 50$, the peak reflectance is calculated to be 77%, with $N = 100$ and 200, the peak reflectances are 98% and 99.99%, respectively. A similar process may be repeated for different corrugation depths which changes the coupling coefficient, and thereby the peak reflectance —however, this also affects the grating bandwidth. A general expression for the full-width half-maximum (FWHM) bandwidth of a uniform grating is given by [46]:

$$\Delta\lambda_{\text{FWHM}} = \lambda_B S \sqrt{\left(\frac{\Delta n_{eff}}{2n_{eff}}\right)^2 + \left(\frac{1}{N}\right)^2} \tag{2.14}$$

Where $S \approx 1$ for gratings with $R \sim 100\%$ and $S \approx 0.5$ for weak gratings.

We see that the bandwidth of the grating increases for low number of periods and higher index difference (i.e. deeper corrugation depth and higher coupling coefficient). Using these simple equations, we can get an intuitive picture of how the reflectance and bandwidth of gratings can be tuned by the coupling coefficient and number of periods. However, a more thorough analysis is possible, if modelling techniques are used.

## 2.7 Bragg Grating Simulation

The transfer matrix method can be used to model the complex transmission and reflection coefficients of a Bragg grating [47]. In the case of sidewall-etched waveguide Bragg gratings, the structure is deconstructed into a series of interfaces and films, as shown in Figure 2-18, where $\mathsf{E}_1$ and $\mathsf{E}_2$ are the electric fields propagating in $n_{\mathrm{eff}_1}$ and $n_{\mathrm{eff}_2}$, respectively. The fields $\mathsf{E}_1'$ and $\mathsf{E}_2'$ are propagating in the opposite direction.

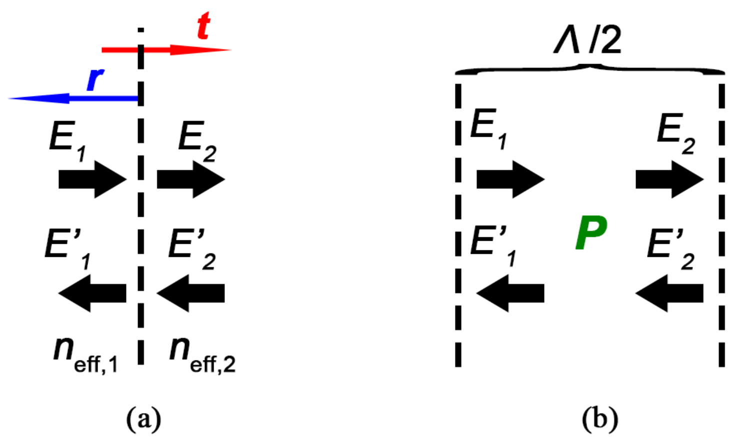


Figure 2-18: The transfer matrix method decomposes the grating into segments and calculates the complex reflection and transmission coefficients of individual (a) $n_{\mathrm{eff}_1}/n_{\mathrm{eff}_2}$ interfaces and (b) $n_{\mathrm{eff}_1}$ or $n_{\mathrm{eff}_2}$ films $\Lambda/2$—thick.

As in equation 2.9, we calculate the reflection coefficient using the Fresnel equations:

$$r_1 = \frac{n_{\mathrm{eff}_2} - n_{\mathrm{eff}_1}}{n_{\mathrm{eff}_1} + n_{\mathrm{eff}_2}} \quad \text{and} \quad r_2 = \frac{n_{\mathrm{eff}_1} - n_{\mathrm{eff}_2}}{n_{\mathrm{eff}_1} + n_{\mathrm{eff}_2}} \tag{2.15}$$

Similarly, the transmission coefficients can be calculated:

$$t_1 = \frac{n_{\mathrm{eff}_1}}{n_{\mathrm{eff}_1} + n_{\mathrm{eff}_2}} \quad \text{and} \quad t_2 = \frac{n_{\mathrm{eff}_2}}{n_{\mathrm{eff}_1} + n_{\mathrm{eff}_2}} \tag{2.16}$$

Using equations 2.15 and 2.16, we are able to construct matrices, $\mathrm{I}_1$ and $\mathrm{I}_2$ to relate the electric field inputs to outputs across an interface:

$$I_1 = \frac{1}{t_1}\begin{bmatrix} 1 & r_1 \\ r_1 & 1 \end{bmatrix} \text{and} I_2 = \frac{1}{t_2}\begin{bmatrix} 1 & r_2 \\ r_2 & 1 \end{bmatrix}; \text{ such that } \begin{bmatrix} E_1 \\ E_1' \end{bmatrix} = I_1 \begin{bmatrix} E_2 \\ E_2' \end{bmatrix} \tag{2.17}$$

The propagating region, or film, is represented in matrices$P_1$ and $P_2$ which each have their own propagation constant, $\beta_1$ and $\beta_2$, where $\beta = 2\pi n_{eff}/\lambda$.

$$P_1 = \begin{bmatrix} e^{\frac{i\beta_1\Lambda}{2}} & 0 \\ 0 & e^{\frac{-i\beta_1\Lambda}{2}} \end{bmatrix} \text{and } P_2 = \begin{bmatrix} e^{\frac{i\beta_2\Lambda}{2}} & 0 \\ 0 & e^{\frac{-i\beta_2\Lambda}{2}} \end{bmatrix}; \text{ such that } \begin{bmatrix} E_1 \\ E_1' \end{bmatrix} = P_1 \begin{bmatrix} E_2 \\ E_2' \end{bmatrix} \tag{2.18}$$

After defining the transfer characteristics of the interfaces and films, we simply multiply all the matrices in the order they appear along the grating to arrive at the transfer matrix, H as shown below in Figure 2-19.

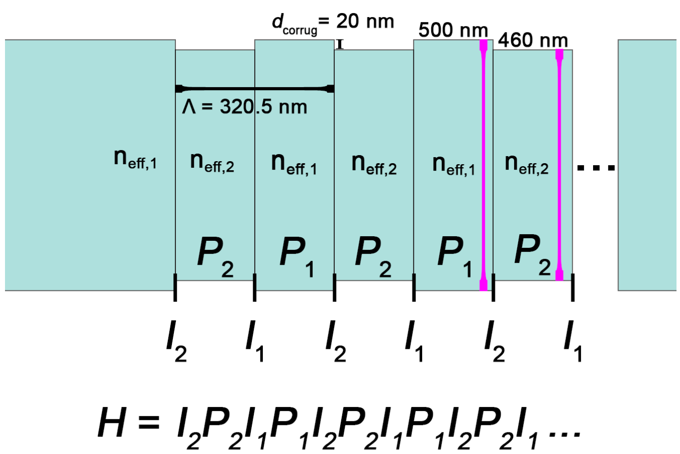


Figure 2-19: The transfer matrix method illustrated for a Bragg grating: the interfaces and films are multiplied along the grating.

The transfer matrix is applied in the following way:

$$\begin{bmatrix} E(0) \\ E'(0) \end{bmatrix} H \begin{bmatrix} E(l) \\ E'(l) \end{bmatrix} \text{where,} H = \begin{bmatrix} H_{11} & H_{12} \\ H_{21} & H_{22} \end{bmatrix} \tag{2.19}$$

Once the transfer matrix is computed, it is easy to determine the complex reflection and transmission coefficients of the Bragg grating using the transfer matrix elements:

$$r = \frac{H_{21}}{H_{11}} \quad \text{and} \quad t = \frac{1}{H_{11}} \tag{2.20}$$

Figure 2-20 (a) shows the reflectance and (b) shows the phase response of gratings with 50, 100, and 200 periods in length, 20 nm corrugation depth, and a grating period of 320.5 nm. As expected from Figure 2.16, the central wavelength is ~1546 nm and peak reflectances of 77.74%, 98.34%, and 99.99% are computed for 50, 100, and 200 periods, respectively; the values are in agreement with those calculated using equation 2.13. As shown in equation 2.14, we expect the bandwidth of the gratings to decrease with increased grating length and is approximately 15 nm. For DWDM applications with 100 GHz channel spacing, each channel is spaced ~0.8 nm apart, as such, the Bragg gratings can accommodate ~18 channels.

## 2.8 Sidewall-Shifted Bragg Gratings

As shown in Figure 2-20, if the amount of grating periods is reduced the reflectance is also lowered. From equation 2.13, we see the peak reflectance is not only dependent on the number of grating periods, but on the coupling coefficient. Previously, in equation 2.10, the coupling coefficient was estimated using the reflection at film interfaces with the effective waveguide indices of the grating segments. Thus, in order to lower the coupling coefficient, we can reduce the corrugation depth, and thereby, the effective index difference between the grating segments. However, in equation 2.14 we see that a smaller corrugation depth will also decrease the bandwidth. For our devices, the corrugation depth is fixed at 20 nm in order to reduce the number of parameter variations. Furthermore, at 20 nm the feature size is already very small and decreasing the corrugation

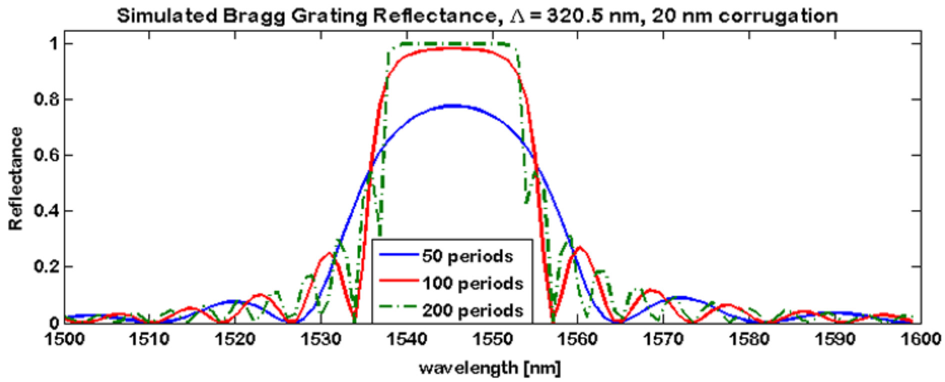


(a)

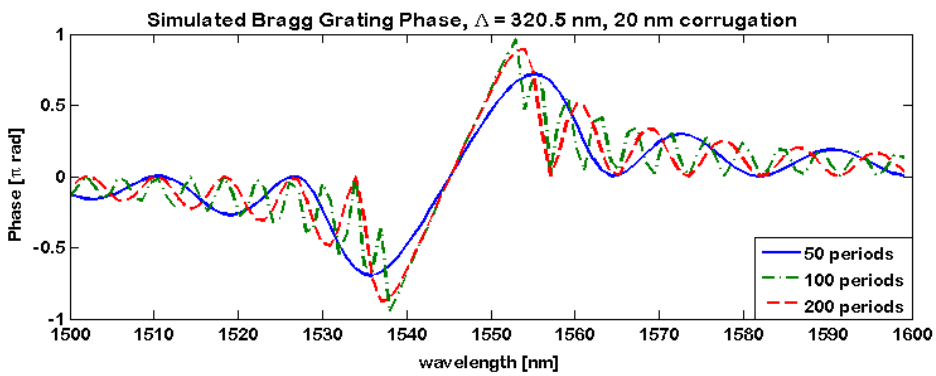


(b)

Figure 2-20: (a) Bragg grating reflectance for sidewall-etched waveguide Bragg gratings with 20 nm corrugation depth and 320.5 nm grating period simulated using transfer matrix method. Dispersive effective indices are simulated using Lumerical MODE —the grating reflectance can be lowered by reducing the number of periods; (b) grating phase is zero at the Bragg wavelength and the strong grating (200 periods) experiences a $2\pi$ rad phase shift over the grating bandwidth.

depth further could increase fabrication inconsistencies.

Due to the grating sensitivity to silicon thickness, smoothening of the sidewall corrugations in lithography, and quantization errors in the shot-pitch in electron-beam fabrication, a recently demonstrated strategy to precisely control the coupling coefficient is to shift one sidewall relative to the other by a fraction of the grating period [48]. A scale diagram of the sidewall-shifted Bragg gratings used in our devices is shown below in Figure 2-21.

As one sidewall is shifted, the coupling coefficient is reduced due to destructive

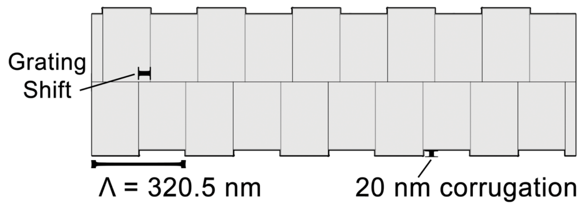


Figure 2-21: Segment of a sidewall-shifted Bragg grating used in our devices.

interference until there is no effective grating at a shift of one half the grating period (i.e. $\Lambda/2$) and it operates as a waveguide. The grating shift is described as a parameter out of 20: at 0/20, there is no grating shift and we have a uniform grating, while at 20/20, the grating is shifted to $\Lambda/2$ and the reflectance should go to zero. Figure 2.22 shows the electric field distribution from FDTD simulations of a sidewall-shifted grating with (a) 0/20 shift and (b) 20/20 shift [48]. Sidewall-shifted gratings will also be implemented in our devices as an alternative means to control the grating reflectance and provide further control over device parameters. Figure 2-22 (c) shows SEM images of sidewall-shifted gratings fabricated using the same E-Beam process as our devices [48].

## 2.9 Summary

This chapter provided background information on silicon photonics necessary to understand the photonic devices detailed in this thesis. The building blocks for silicon photonic devices and circuits are also introduced, such as waveguides, couplers, and Bragg gratings. As silicon photonics matures, designs from process development kits and research prototypes enable a modular approach composed of key photonic components; the ones relevant to our devices are outlined in this chapter. Section 2.1 introduced integrated photonics platforms and explains the choice of the SOI platform. Fabrication tools for silicon photonics Deep-UV lithography and electron beam lithography are introduced and compared in Section 2.2. The wires of silicon photonics, waveguides, are introduced in section 2.3 and the concepts of guiding light; material, effective and group indices; optical

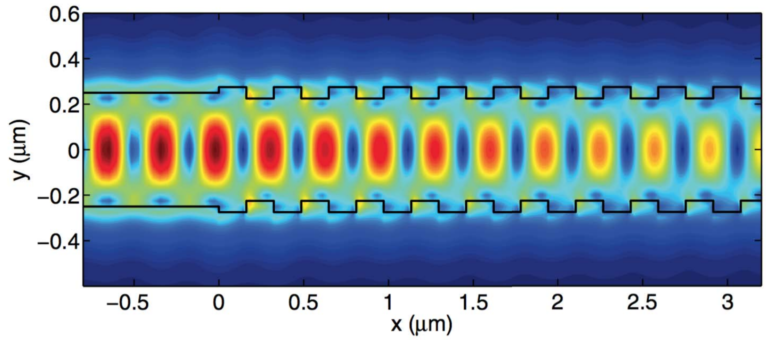


(a)

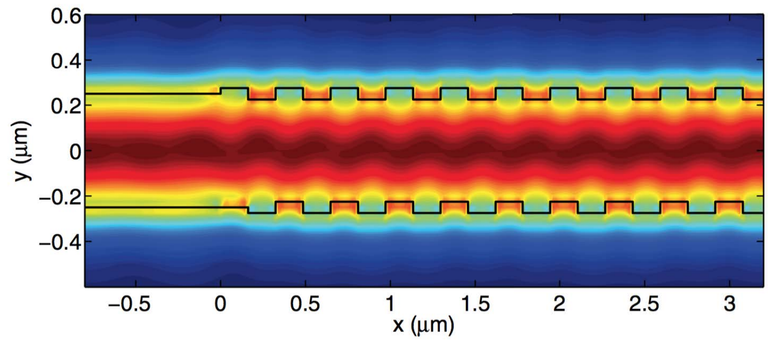


(b)

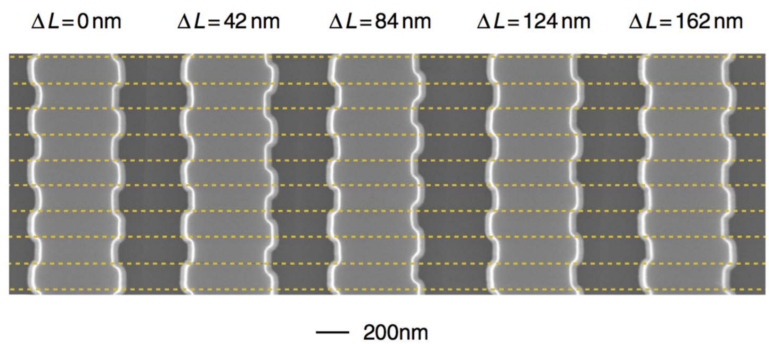


(c)

Figure 2-22: Electric field distribution from FDTD simulations: (a) uniform grating and (b) sidewall-shift of half the grating period (shift parameter of 20/20), resulting in complete destructive interference; (c) SEM images of sidewall-shifted Bragg gratings with various offsets , $\Delta L$ [48].

modes and effect of waveguide geometry; and optical attenuation in silicon waveguides are detailed. Section 2.4 outlined SOI waveguide couplers and provides information on the Y-branches and multimode interference couplers used in our devices. Low fibre coupling losses is essential to on-chip device performance, as such, Section 2.5 compared two common optical fibre coupling methods: edge coupling and vertical grating couplers. Due to relaxed coupling tolerances, quicker alignment and testing, and the ability to place them anywhere on the chip, we use vertical grating couplers for the devices detailed in this thesis. Section 2.6 introduced waveguide Bragg gratings and provided background theory on grating design, while section 2.7 detailed Bragg grating simulation using the transfer matrix method and presented simulation results for gratings typical of the ones used in our devices. Finally, section 2.8 introduced an alternative means for controlling the coupling coefficient of sidewall corrugation waveguide Bragg gratings by shifting one sidewall to induce destructive interference in the grating.

# Chapter 3

# Gires-Tournois Interferometers in SOI

This chapter presents simulation and experimental results of an integrated GTI on the SOI platform based on sidewall corrugated waveguide Bragg gratings. The GTI is introduced in section 3.1 and section 3.2 provides background on the design of our GTIs as well as the different configurations that are employed. In section 3.3, simulation results of the GTIs are presented and the effects of design parameters are discussed. Fabrication of the devices and the experimental setup used for device characterization is detailed in section 3.4. Measurement results are presented in section 3.5 and are discussed and compared with simulation results. Section 3.6 concludes the chapter on GTIs and provides recommendations for future designs.

## 3.1 Introduction to Gires-Tournois Interferometers

The GTI is a Fabry-Perot cavity with one mirror of low reflectance, $\mathsf{R}_1$, and another mirror of ~100% reflectance, $\mathsf{R}_2$. The original design proposed by in 1964 by François Gires and Pierre Tournois consists of a transparent plate with two reflecting surfaces, as shown in Figure 3-1 [49].

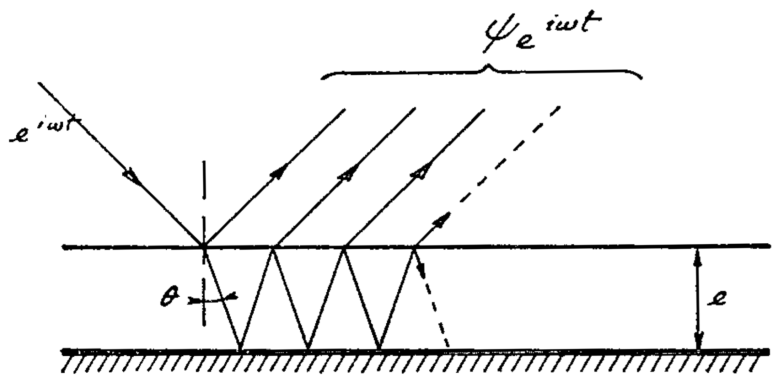

Figure 3-1: Original ray-diagram for a GTI: for a fixed wavelength, the complex amplitude of a plane wave, $\psi$, has a phase-shift that varies periodically with respect to the incidence angle, $\theta$, over a period determined by the plate thickness, $e$ [49].

The reflected plane wave is given by [49]:

$$\psi \cdot e^{i\omega t} = \frac{-r + e^{i\omega\delta}}{1 - r \cdot e^{i\omega\delta}} \cdot e^{i\omega t} \quad \text{and} \quad \delta = \frac{2en\cos\theta}{c} \tag{3.1}$$

where $\psi$ is the complex amplitude of the reflected plane wave, $\omega$ is the angular frequency of the plane wave, $r$ is the reflection coefficient of the air to plate interface (if $r$ is real, then $|r| = \sqrt{R}$), and $e$ is the plate thickness (as shown in Figure 3-1), $\theta$ is the incident angle of light on the plate, $n$ is the refractive index of the plate, and c is the speed of light in a vacuum.

If the angle of incidence of the light is fixed, the complex reflection coefficient of the GTI is periodic with respect to the wavelength. Figure 3-2 shows the real and imaginary components of the complex reflection coefficient a GTI with normal incidence for front-mirrors with reflectances of (a) 5.5% and (b) 50% (assumed to be real and non-dispersive) and an index of 2.443 —the previously determined effective index of a 500 nm $\times$ 220 nm SOI waveguide around 1546 nm.

The GTI reflectance is given by $R_{GTI} = |r_{GTI}|^2$ . In the ideal, lossless, case, GTIs exhibit 100% reflectance across all wavelengths and the device acts as a phase-dispersive mirror. Between each resonance peak a $2\pi$ phase-shift occurs. By changing the re-

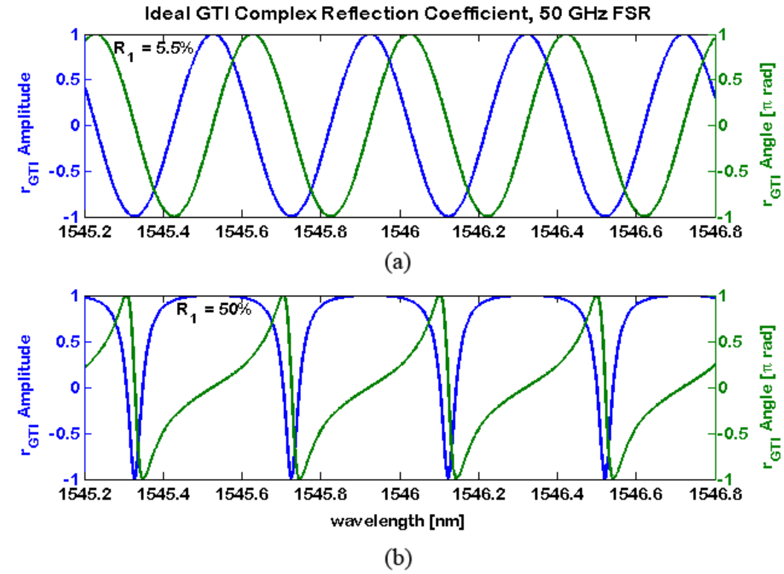


Figure 3-2: Complex reflection coefficient of an ideal GTI with 50 GHz FSR, refractive index of 2.443, and front-mirror reflectances of (a) 5.5% and (b) 50%.

flectance of the front-mirror, the phase, and thereby, the group delay can be controlled. GTIs in free-space configurations have been demonstrated and find use in femtosecond pulse compression [50]. Fibre-based GTIs were later demonstrated for dispersion and dispersion-slope compensation in wavelength-division multiplexing (WDM) applications [51]. A schematic of free-space and fibre-optic GTIs are shown in Figure 3-3.

An integrated configuration of a GTI on the SOI platform has also been demonstrated in a multimode waveguide using a cleaved facet for the low-reflectance mirror and a deep-etched grating for the high-reflectance mirror, as shown in Figure 3-4 (a). The device exhibits the desired phase-response, but the losses are too high for practical use in dispersion compensation applications, as such, the authors suggest the SOI GTI could be used in an Michelson-GTI (MGTI) for channel interleaving applications [53]. The measured reflectance is shown in Figure 3-4 (b). The losses at the resonance peaks are due to a combination of coupling losses, propagation loss, and polarization dependent losses (PDL).

In the configuration shown in Figure 3-4 (a), a cleaved facet for the low-reflectance

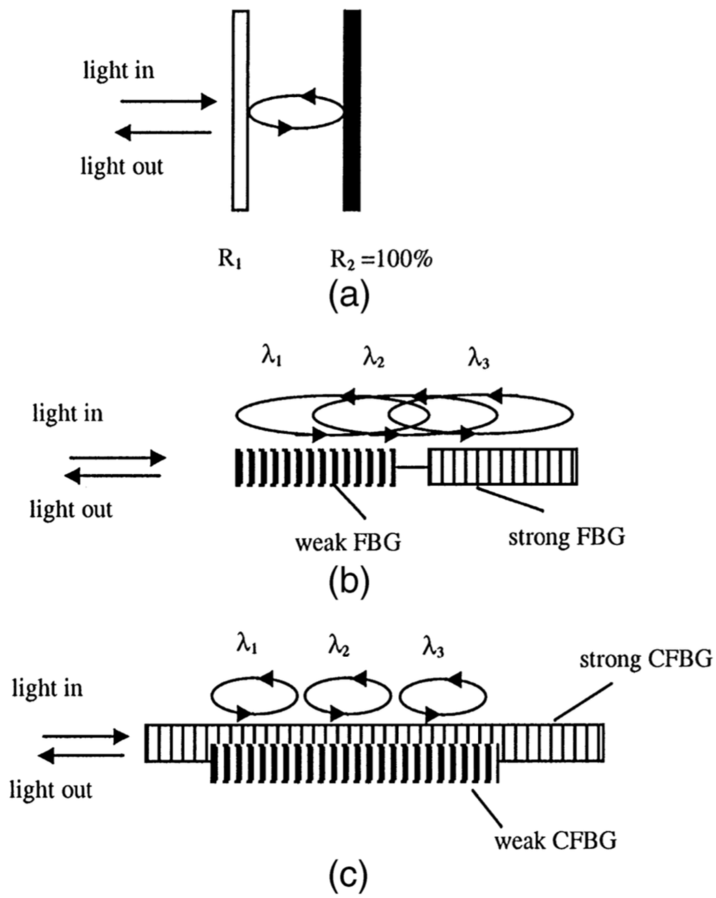


Figure 3-3: (a) Bulk optic GTI with R1 < 100%, (b) GTI formed by uniform fibre Bragg gratings, (c) GTI formed by overlapping chirped fibre Bragg gratings [52].

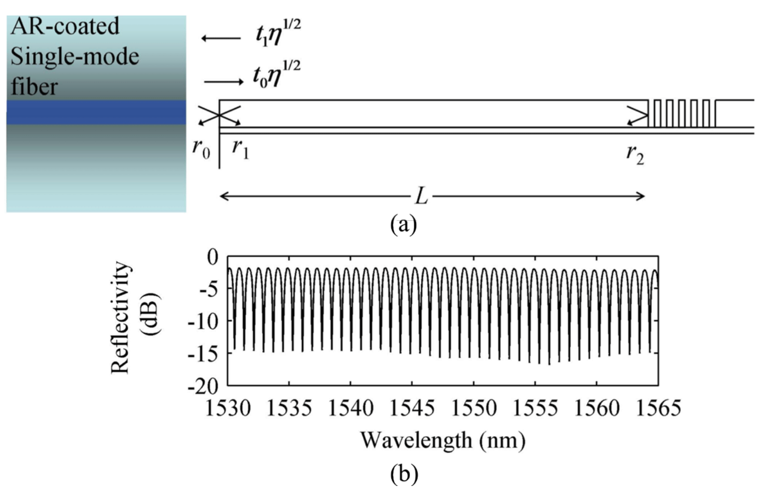


Figure 3-4: Measured 100 GHz SOI-GTI reflectance from St. Gelais *et al.* There are wavelength-dependent losses of ~ 13 dB at the resonance peaks due to coupling losses, propagation loss, and PDL [53].

mirror of a GTI enables broadband reflectance of ~55% [53]. However, the cleaved facet would require an MGTI to be configured off-chip and the use of a multimode waveguide for the GTI cavity further reduces the ability integrate the device into PICs. In order to create a GTI that can be used in PICs, a new integrated solution based on single-mode waveguides is required.

## 3.2 Gires-Tournois Interferometer Design

We demonstrate a novel GTI design based on integrated sidewall Bragg-gratings in a single-mode waveguide. The grating parameters can be selected to achieve the desired reflectances of both mirrors in the GTI. The single-mode strip waveguides enables integration into PICs and facilitates the use of previously designed silicon photonic components, such as vertical grating couplers (VGCs) and Y-Branches. Our GTI has an approximate footprint of 0.28 mm $\times$ 1 mm for a device with 50 GHz free spectral range (FSR). VGCs are used for fibre-coupling to the chip and have relaxed alignment tolerances and quicker testing than edge-coupled devices [54]. This design allows for compact, on-chip, integration into a MGTI configuration leveraged by components on the SOI platform. Furthermore, by using Bragg gratings for mirrors, non-uniform grating profiles, such as chirped, sampled, or apodized gratings, could be implemented in future devices to reduce phase noise, tune the spectral and dispersion profiles, and enable advanced design flexibility over existing GTI and MGTI configurations [32].

When a Bragg grating with high reflectance and another with low reflectance are separated by section of waveguide, a GTI is formed. A schematic of our SOI GTI is shown below in Figure 3-5. The following expression is used to determine the complex GTI reflection coefficient [53]:

$$r_{GTI} = r_0 + \frac{t_0 t_1 r_2 \gamma e^{-2i\beta d_{GTI}}}{1 - r_1 r_2 \gamma e^{-2i\beta d_{GTI}}} \tag{3.2}$$

where $\beta = 2\pi n_{eff}/\lambda$ is the propagation constant of the waveguide, $d_{GTI}$ is the cavity spacing, $\gamma = \exp(-2\alpha_{wg} d_{GTI})$ is the the propagation loss for one round trip, $\alpha_{wg}$ is the attenuation coefficient of the silicon waveguide, $r_0 = r_1$ is the complex reflection coefficient of the front-grating, $t_0 = t_1$ is the transmission coefficient through the front-grating, and $r_2$ is the reflection coefficient of the back-grating. The cavity length of the GTI, $d_{GTI}$, determines the free spectral range (FSR) and the strength of the low reflectance grating determines the finesse, and thereby the extinction ratio. In order to function as an interleaver, the GTI FSR must be the same as the channel spacing of the frequency interleaved signal (e.g. 50 GHz). Additionally, in order to obtain box-like passbands in the interleaver response, the reflectances of the front-gratings of the GTI must different, thus control over the grating reflectance is critical to our design.

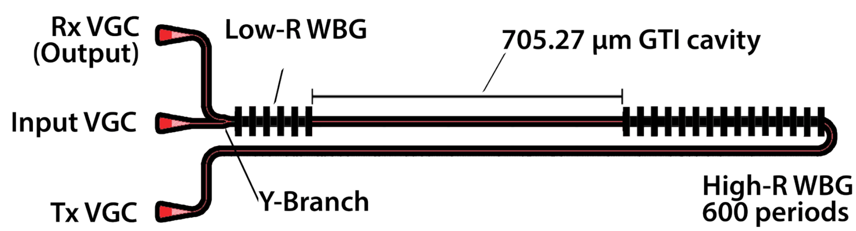


Figure 3-5: Schematic of GTI in SOI based on sidewall corrugated Bragg gratings.

As discussed in sections 2.7 and 2.8, we use two methods to control the reflectance of our gratings: changing the number of grating periods and offsetting the sidewall corrugations by a fraction of the grating period —both configurations are used in our GTI designs and are compared with each other and simulation results.

## 3.3 Gires-Tournois Interferometer Simulation

In order to simulate our grating-based GTI, the reflection and transmission coefficients of the Bragg gratings are determined using the transfer matrix method, as detailed in section 2.7 and inserted into equation 3.2 along with the dispersive effective index computed using Lumerical MODE and a waveguide propagation loss of 3 dB/cm —a value typical for the electron beam process used [28]. Figure 3-6 shows simulation results of the complex GTI reflection coefficient when gratings are used instead of ideal mirrors. The simulated results are similar to the ideal case shown in Figure 3-2, except that the passbands are less symmetric the further away from the Bragg wavelength, as shown in Figure 3-6 (c). This non-uniformity is due to the fact that the Bragg gratings have a finite bandwidth and a rounded passband. Furthermore, the addition of 3 dB/cm losses reduces the range of both the amplitude and phase angle components of the reflection coefficient.

In previous free space MGTI configurations, optimal values for front mirror reflectances of 50.5% and 5.5% have been reported [55]. We aim to achieve these reflectances by modifying both the grating length and sidewall-shift. If a 20 nm corrugation depth is used (waveguide segments with widths of 500 nm and 460 nm), TMM simulation results show that 29 and 7 periods are required for gratings of ~50.5% and 5.5% peak reflectance, respectively. Figure 3-7 shows simulation results for GTIs with front-grating reflectances of ~5.5% and ~50%; the cavity length is 705.267 μm and a 321.5 nm grating period with 20 nm corrugation depth is used.

Although we expect a uniform reflectance from an ideal GTI, as with the reflectance of the GTI shown in Figure 3-4 (b), there are losses at the resonance peaks. For the GTI with a front-grating reflectance of 5.5%, an extinction ratio of 0.8 dB is simulated. When the GTI has a front-grating reflectance of 50%, the extinction ratio is 5.7 dB. The responses are periodic with an FSR of ~0.4 nm, corresponding to 50 GHz channel spacing for the wavelengths of interest. Both GTIs have a filter bandwidth of 17 nm which can

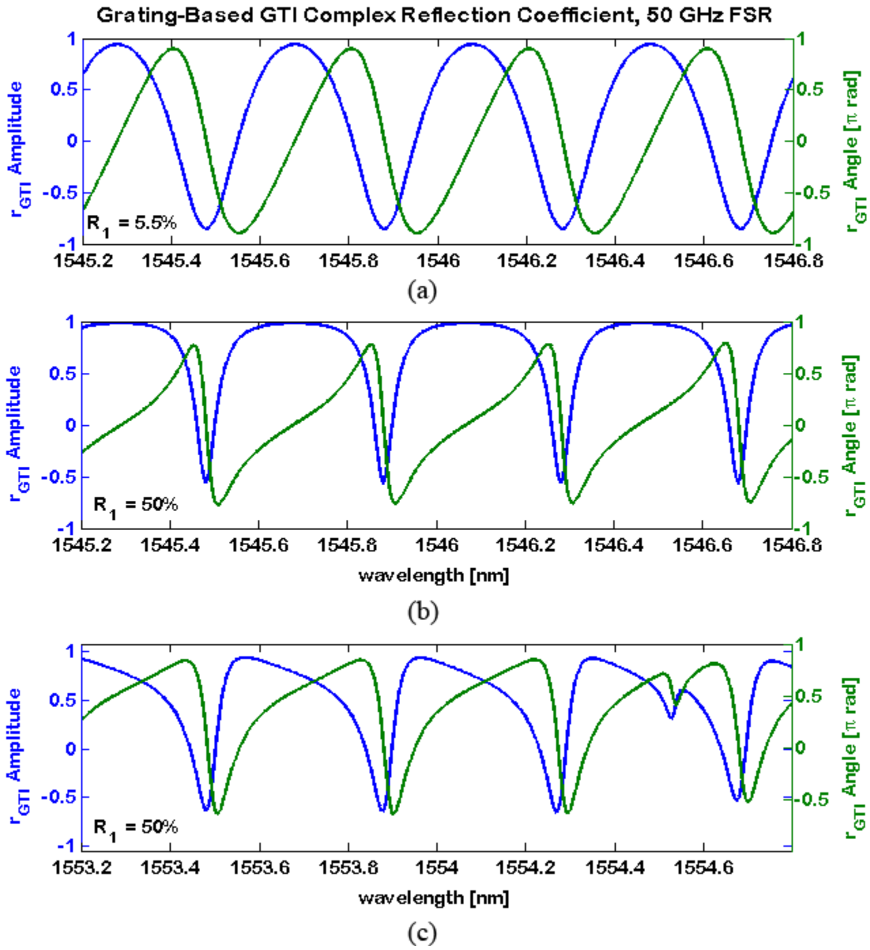


Figure 3-6: Simulated complex GTI reflection coefficient using TMM grating coefficients, the dispersive effective index, 3 dB/cm loss, a cavity spacing of 705.27 µm, and front-grating reflectances of (a) 5.5% and (b) 50%; (c) at longer (or shorter) wavelengths than the Bragg wavelength, the coefficient has asymmetric passbands.

accommodate 42 DWDM channels with 50 GHz spacing.

The finesse, defined as the FSR divided by the full-width half-max (FWHM), decreases as the cavity losses are increased [23]. In the simulations, two types of losses make up the cavity loss: the propagation loss (assumed to be constant at 3 dB/cm) and the coupling losses, which in our case is determined by the front grating reflectance. As such, the finesse, and thereby the extinction ratio, is decreased as the amount of periods in the front grating is decreased, as observed in Figure 3-7. PDL is not included in the losses, because the VGCs used only accept TE polarization and the waveguides are designed to

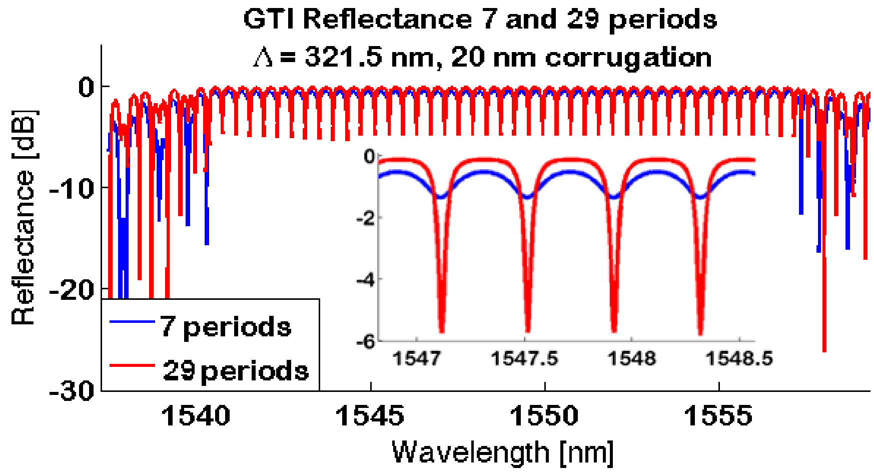


Figure 3-7: Simulated reflectances of GTIs with front mirror reflectances of 5.5% and 50%.

only support the fundamental TE mode. Figure 3-8 shows the effect of propagation loss on the reflectance of a GTI with a front-grating of 50% reflectance. As the propagation loss increase from 3 dB/cm to 5 dB/cm, the extinction ratio increases from ~5 dB to ~9 dB. In the lossless case (0 dB/cm), 100% reflectance is simulated across the wavelengths of interest and there are no troughs at the resonant wavelengths.

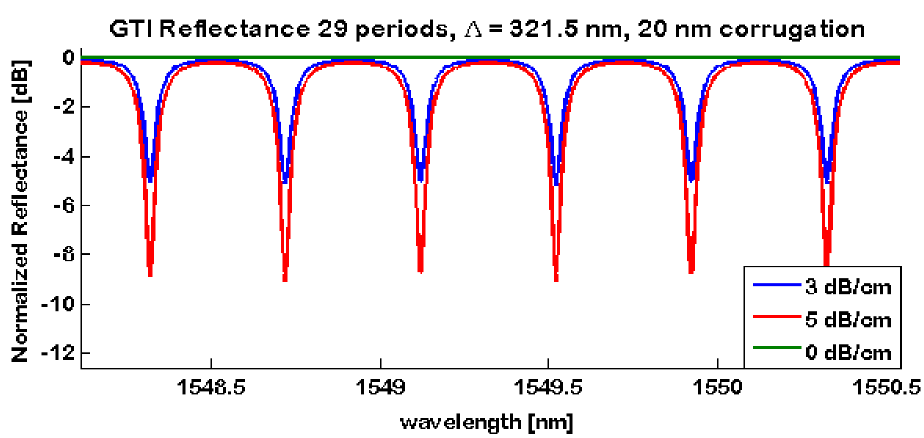


Figure 3-8: Effect of propagation loss on GTI reflectance.

## 3.4 Fabrication and Experimental Setup

The devices were fabricated by Richard Bojko at the University of Washington Nanofabrication Facility using 100 kV Electron Beam Lithography [28] . The fabrication used silicon-on-insulator wafer with 220 nm-thick silicon on 3 μm thick silicon dioxide. The substrates were 25 mm squares diced from 150 mm wafers. After a solvent rinse and hotplate dehydration bake, hydrogen silsesquioxane resist (HSQ, Dow-Corning XP-1541-006) was spin-coated at 4000 rpm, then hotplate baked at 80°‘C for 4 minutes. Electron beam lithography was performed using a JEOL JBX-6300FS system operated at 100 kV acceleration voltage, 8 nA beam current, and 500 μm exposure field size. The machine grid used for shape placement was 1 nm, while the beam stepping grid, the spacing between dwell points during the shape writing, was 6 nm. An exposure dose of 2800 $\mu C/cm^2$ was used. The resist was developed by immersion in 25% tetramethylammonium hydroxide for 4 minutes, followed by a flowing deionized water rinse for 60 s, an isopropanol rinse for 10 s, and then blown dry with nitrogen. The silicon was removed from unexposed areas using inductively coupled plasma etching in an Oxford Plasmalab System 100, with a chlorine gas flow of 20 sccm, pressure of 12 mT, ICP power of 800 W, bias power of 40 W, and a platen temperature of 20°C, resulting in a bias voltage of 185 V. During etching, chips were mounted on a 100 mm silicon carrier wafer using perfluoropolyether vacuum oil.

The final chip is cleaned in acetone and isopropyl alcohol in order to remove photoresist and is placed on a optomechanical stage. A four-port fiber ribbon array is used in order to couple light to the chip as shown in Figure 3-9.

On the fiber ribbon array, two ports are used for the measurements: one for the laser input and one for the GTI reflection output. The fiber ribbon array and optomechanical stage are adjusted in order to optimize coupling between the fiber ribbon array and the VGCs on the silicon photonic chip. The relaxed alignment tolerances of the VGCs makes

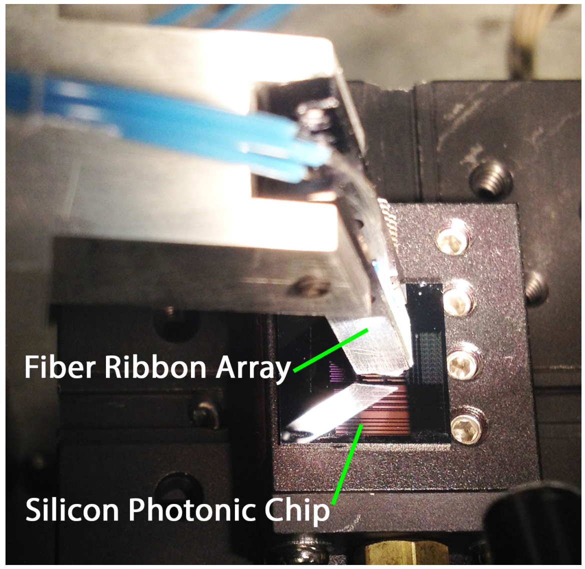


Figure 3-9: Photograph of optical coupling setup showing fiber ribbon array and silicon photonic chip.

it easier to switch between devices on the chip. A video camera with a telecentric lens is used for monitoring the chip and fiber ribbon array.

Figure 3-10 shows a block diagram of the experimental setup used to measure GTI reflectance spectra. A tunable laser (Keysight 8164B) is swept over the telecom C-band (1530 nm to 1570 nm) and the output of the device under test (DUT) is measured using a fiber optic power meter (ILX Lightwave FPM-8200). A polarization rotator is used to match the state of polarization of the signal in the optical fibres to the TE mode of the waveguides.

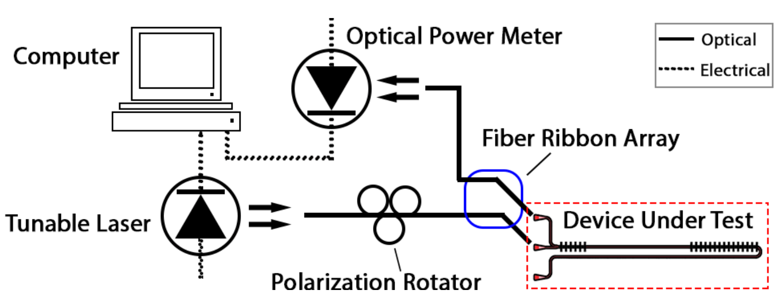


Figure 3-10: Experimental setup for measuring GTI reflectance spectra.

## 3.5 Gires-Tournois Interferometer Measurement Results

In order to separate the VGC response from that of the GTIs, the VGC spectrum is measured using a test structure that consists of two VGCs connected by a short waveguide. The measured results for the same VGC design as in Figure 2-14 is shown below in 3-11. The minimum insertion loss of 19.5 dB occurs at wavelengths near 1549 nm and is higher than those reported for the sub-wavelength VGC [36]. The insertion loss can be reduced by tuning the angle of the fibre ribbon array with respect to the chip, however this typically shifts the VGC spectrum.

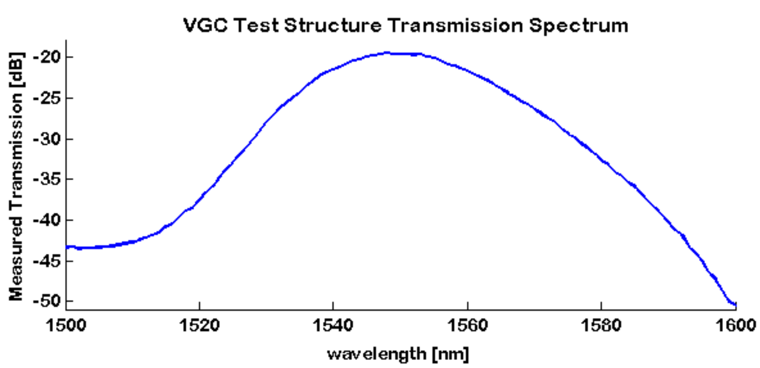


Figure 3-11: Measured transmission spectrum of VGC test structure.

The VGC data is used as a baseline and is subtracted from measurements in order to normalize the results. Measured and simulated results for Bragg grating test structures with 105 and 700 periods are shown in Figure 3-12. When the number of periods is reduced from 700 to 105 periods, the extinction ratio of the transmission spectrum is reduced from ~30 dB to ~7 dB. However, the simulation data shows a wider bandwidth and higher extinction ratio than the measured results, meaning the coupling coefficient of the measured results is smaller than predicted through simulations; the simulated bandwidth of a 700 period grating with 320 nm corrugation depth is 16 nm, while the measured bandwidth is 7 nm. The high reflectance in the simulated gratings when compared to measurements is likely due to the fact that the transfer matrix method only considers reflection and transmission of thin-films and assumes a normal angle of incidence, which would result in a higher coupling coefficient than the true case of integrated waveguides. Furthermore, by using a 6 nm stepping grid in the E-beam writing process, the edges of the Bragg grating may be smoothened and can be seen in SEM images of Figure 2-22 (c).

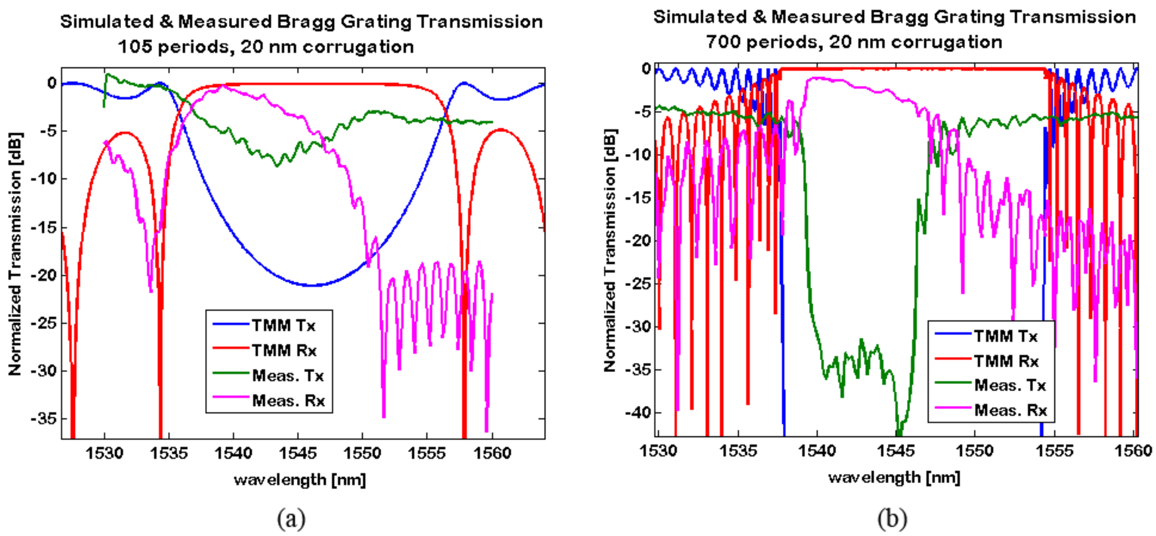


Figure 3-12: Simulated (TMM) and measured Bragg grating transmission (Tx) and reflection (Rx) spectra for sidewall waveguide Bragg gratings with 320.5 nm periods, 20 nm corrugation depth, and (a) 105 periods and (b) 700 periods.

In order to correlate the response of the GTIs with uniform Bragg gratings to the simulations, the reflectance is measured for devices with 100 to zero front-grating periods and the extinction ratios are matched to the simulated response of a GTI with 29 front-grating periods. While it may seem more direct to compare grating test structures, the dips in the transmission response are too small for accurate measurement. Figure 3-13 (a) shows the measured results for a GTI with 100 front-grating periods and compares it with simulated results of a GTI with 29 front-grating periods; from the inset, it is evident that a GTI with 100 front-grating periods corresponds has ~50% reflectance in the the front-grating and has an extinction ratio of ~5 dB. Figure 3-13 (b) shows high-resolution measurement results for GTIs with 100, 70, 50, and 30 period front-gratings. Similar to that predicted by the simulations in Figure 3-7, as the amount of front-grating periods is decreased, the extinction ratio of the GTIs decreases and the square shape of the GTI passbands become more rounded-off.

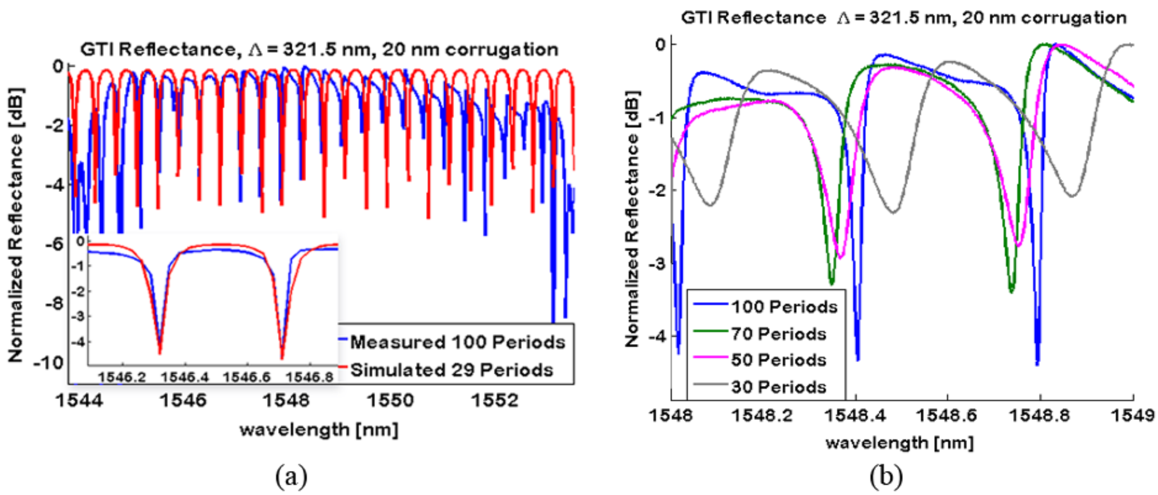


Figure 3-13: (a) Measured and simulated results of a GTI with 100 and 29 front- grating periods, respectively; (b) effect of number front-grating periods; all devices have $\Lambda$ = 321.5 nm, 20 nm corrugation depth, 705.267 μm cavity length, and 700 back-grating periods.

If shifted gratings are used, an extinction ratio of ~5 dB and a spectral response similar to the simulated GTI with 50% front-mirror reflectance is observed for a grating of 200 periods and a shift parameter of 15/20, as shown in Figure 3-14. Thus, by adjusting the amount of grating periods or the shift-parameter in the front-grating of the GTI, we are able to control the reflectance of the grating, and thereby the extinction ratio of the GTI.

The measurement results for GTIs with 100 and 200 front-grating periods and shift parameters of 1/20, 5/20, 13/20, 16/20, and 19/20 are shown below in Figure 3-15.

Figure 3-16 compares the extinction ratio of the GTIs, measured near the Bragg wavelength, when the amount of periods is in the front grating is reduced with (a) no sidewall shift, (b) 100 front-grating periods and an increasing sidewall shift, and (c) with

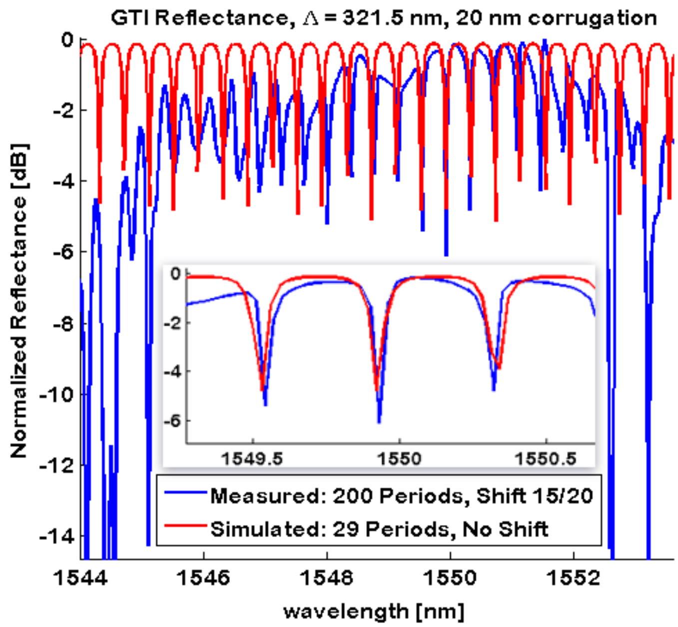


Figure 3-14: Measured and simulated results of a sidewall-shifted GTI with 200 front-grating periods and a shift parameter of 15/20; $\Lambda = 321.5$ nm, 20 nm corrugation depth, 705.267 μm cavity length, and 700 periods in the back-grating

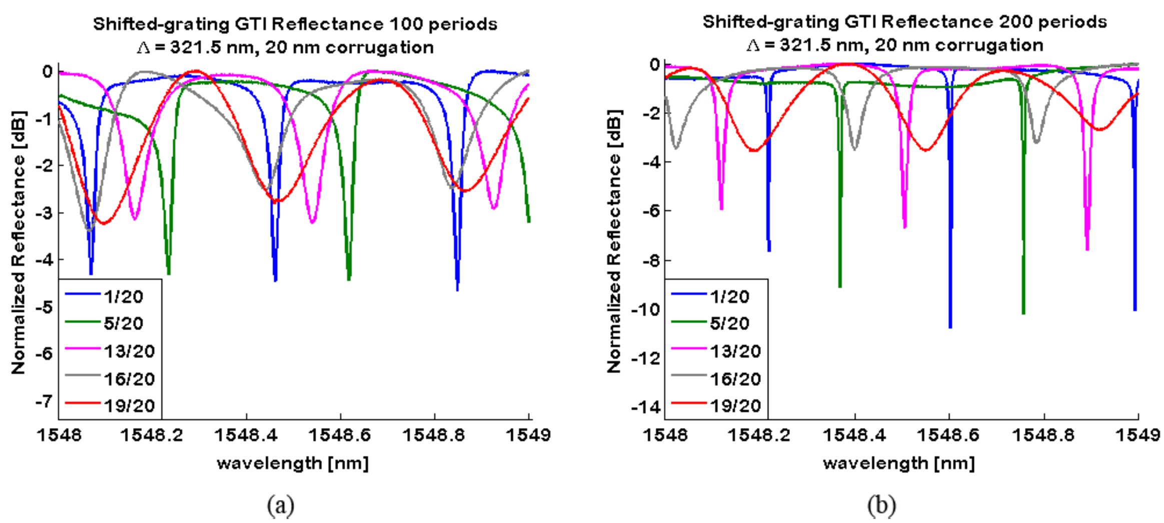


Figure 3-15: Measured sidewall-shifted GTI reflection spectra for GTIs with (a) 100 and (b) 200 front-grating periods, 700 back-grating periods, 20 nm corrugation depth, $\Lambda = 321.5$ nm, a cavity length of 705.27 μm, and various shift parameters.

200 front-grating periods and an increasing sidewall shift. Unlike the GTI simulations, the measured responses are not consistent across the bandwidth of the gratings used in the GTIs.

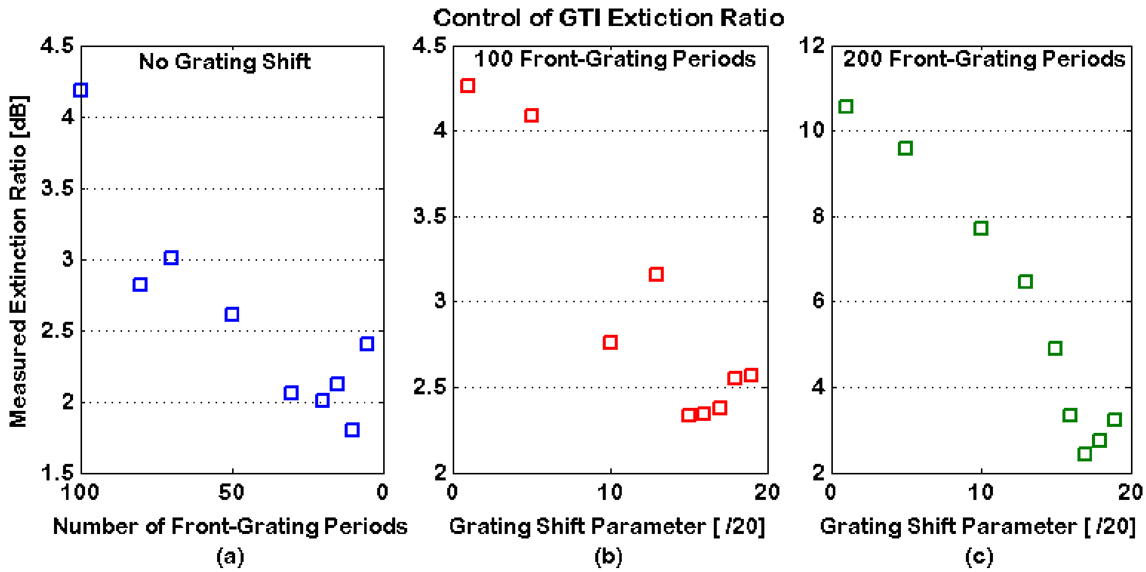


Figure 3-16: Approximate measured extinction ratio of GTI devices for various front-grating lengths and sidewall shifts.

Furthermore, in Figure 3-16, the extinction ratio does not go below ~2 dB and the trend of less grating periods or more shift leading to a smaller extinction ratio stops. In fact, when a device is measured that has no periods in the front grating (i.e. just the GTI cavity waveguide and the back-grating), a periodic response is still observed with up to 3 dB extinction ratio, as shown in Figure 3-17. Because the cavity response seen in Figure 3-17 has the same FSR of the GTIs, the ripples can be attributed to reflections caused by the Y-Branch, and the impact of this can be seen in all of the measured GTI spectra. The limited bandwidth is attributed to both the finite bandwidth of the Bragg gratings used in the GTIs and the reflection from the Y-branch.

## 3.6 Conclusion

The GTI has been around for decades and has found many applications using free-space and fibre-based configurations. If GTIs can be used easily integrated into silicon photonic circuits, then they could be used as key components in other silicon photonic devices,

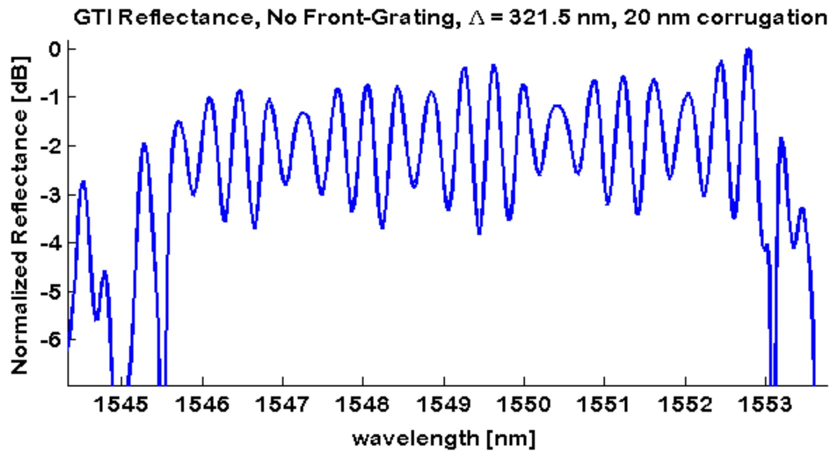


Figure 3-17: Measured reflectance of a GTI with no front-grating periods; the back-grating has $\Lambda = 321.5$ nm, 20 nm corrugation depth, 705.267 µm cavity length, and 700 periods in the back-grating.

such as MGTIs for WDM channel interleaving applications. However, designing MGTIs requires a high level of control in the GTI spectral response. We demonstrate a GTI with a flexible design by using two configurations, i.e. reducing the number of periods in the front-grating or by offsetting the sidewall corrugations, and show it is possible to control the extinction ratio. Although simulations predicted stronger coupling in the sidewall Bragg gratings, the trends in controlling the GTI properties are as expected, until an extinction ratio of ~2 dB. The GTIs with low (or no) front-grating reflectance show a periodic response likely caused by reflections from the Y-Branch. Since front-grating reflectances of ~5.5% and 50% have previously been shown to be optimal for MGTI interleavers, it is recommended that front-gratings with ~100 periods be used for ~50% reflectance and no front-grating (as in Figure 3-17) be used for the GTI with front-grating reflectance of ~5.5%. It is also recommended that designs using multi-mode interference couplers as an alternative to the Y-branch be used in case there is reduced reflectance causing the cavity response. By utilizing sidewall-corrugated Bragg gratings in single-mode SOI waveguides to create GTIs, they become devices with highly-flexible designs, a compact form, and can be easily integrated into other devices and photonic circuits.

It is recommended that future work on our GTIs include methods to improve the device bandwidth, which is limited by the reflectances of the Bragg gratings. Due to the design flexibility of the sidewall gratings, non-uniform grating profiles can be investigated.

# Chapter 4

# Michelson-Gires-Tournois Interferometers in SOI

This chapter integrates the GTI devices of chapter 3 into a simple silicon photonic circuit designed to interleave channels in wavelength-division multiplexing applications using a design known as an MGTI. Section 4.1 introduces optical interleavers and previous efforts to integrate them on the silicon-on-insulator platform while section 4.2 details the MGTI design. Simulation results of grating-based MGTIs are presented in section 4.3 and are compared to measured results in section 4.4. Conclusions and recommendations based on the results are drawn in section 4.5.

## 4.1 Optical Interleavers

Wavelength division multiplexing (WDM) enables high data capacity over optical fibres and waveguides by combining multiple signals modulated on different wavelengths, or carriers. Each of the carrier wavelengths is considered a channel. Depending on the system and application, the channel spacing is varied; for example, modern dense wavelength division multiplexing (DWDM) systems have 12.5, 25, 50, or 100 GHz channel spacing, as defined by recommendation ITU-T G.694.1 [56]. In order to multiplex WDM channels with different spacing (e.g. two data streams with 100 GHz channel spacing multiplexed to a data stream with 50 GHz channel spacing), optical interleavers may be employed. Optical interleavers are periodic bandpass filters that are essential components of modern DWDM systems as an economic method to (de)multiplex even and odd channels, route them to other locations in a network, and filter the signal to reduce the crosstalk [57]. Interleavers and de-interleavers are passive devices with 3 ports, as shown in Figure 4-1 (a) and (b), respectively.

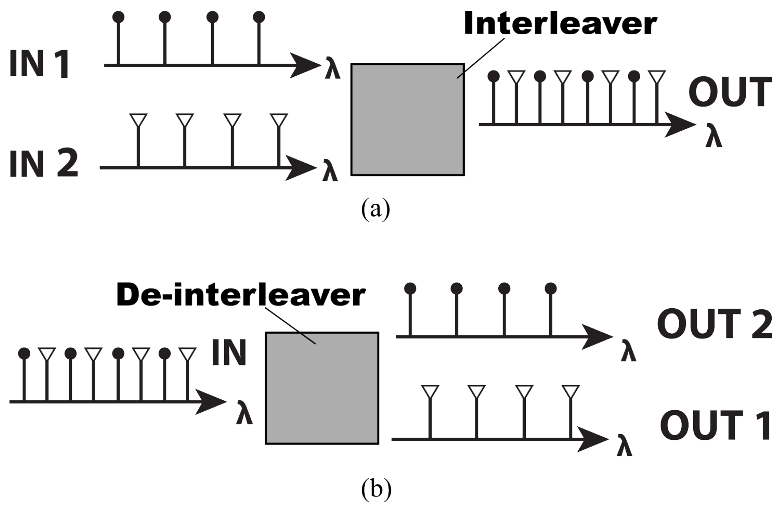


Figure 4-1: (a) Interleaving and (b) de-interleaving channels in a wavelength division multiplexing system.

Interferometric structures are selected for interleavers due to their inherent periodic spectral response. The two simplest designs are the Mach-Zehnder interferometer (MZI) and the Michelson interferometer (MI), shown in Figure 4-2 (a) and (b), respectively. In both configurations, the input light is split using a 50/50 directional coupler, light in one arm undergoes a phase shift, and then the light in both arms is recombined. Y-branches may be used for the MZI, and MMI couplers may be used for both MZI and MI configurations. The light experiences a differential phase shift, , between the long arm, with length , and the reference arm, with length , that upon recombining creates a periodic power transmittance given by equation 4.1 [23]. The sign is dependent on the type of couplers used and whether the interferometer is configured as an MZI or MI. The response is sinusoidal with respect to wavelength if the path-length difference is fixed, as shown in Figure 4-2 (c).

$$\mathsf{T} = 1 - 0.5 \cdot (1 \pm \cos \Delta\varphi) \tag{4.1}$$

Both the MZI and MI function as optical (de-)interleavers if directional couplers or MMI couplers are used. In Figure 4-2, the inputs and outputs are configured for de-interleaving applications; e.g. a WDM signal with 50 GHz channel spacing (~0.4 nm at wavelengths near 1550 nm) is at the input, and each of the two outputs have 100 GHz channel spacing (~0.8 nm at wavelengths near 1550 nm). Figure 4-2 (c) shows the output of a MZI/MI interleaver as the blue and red traces. In order to interleave two 100 GHz WDM channels, the inputs and outputs are simply switched.

The output is a periodic filter –in this case one with a sinusoidal profile. The passbands of the spectra should be centered at the wavelengths used by the ITU grid. If functioning as an interleaver, it is important that the neighbouring channels, in this case the red and blue traces in Figure 4-2 (c), have a high levels of isolation between channels in order to avoid crosstalk which can lead to errors in the data. In the case of the MZI or MI interleaver spectrum shown in Figure 4-2 (c), the 20 dB bandwidth is much wider than the 3 dB bandwidth, meaning that more optical power from neighbouring channels can interfere with the signal in a given channel. Furthermore, with a small 3 dB bandwidth, the rounded passbands could cause insertion loss on wavelengths away from the center of the passbands. Thus, the ideal interleaver filter spectrum would be one with a box-like profile –high extinction ratio between channels and flat passbands and a 20 dB bandwidth the same (or slightly wider) than the 3 dB bandwidth. In order to generate box-like spectra, other interleaver designs are necessary.

By cascading MZIs, and choosing the correct path-length differences, it is possible

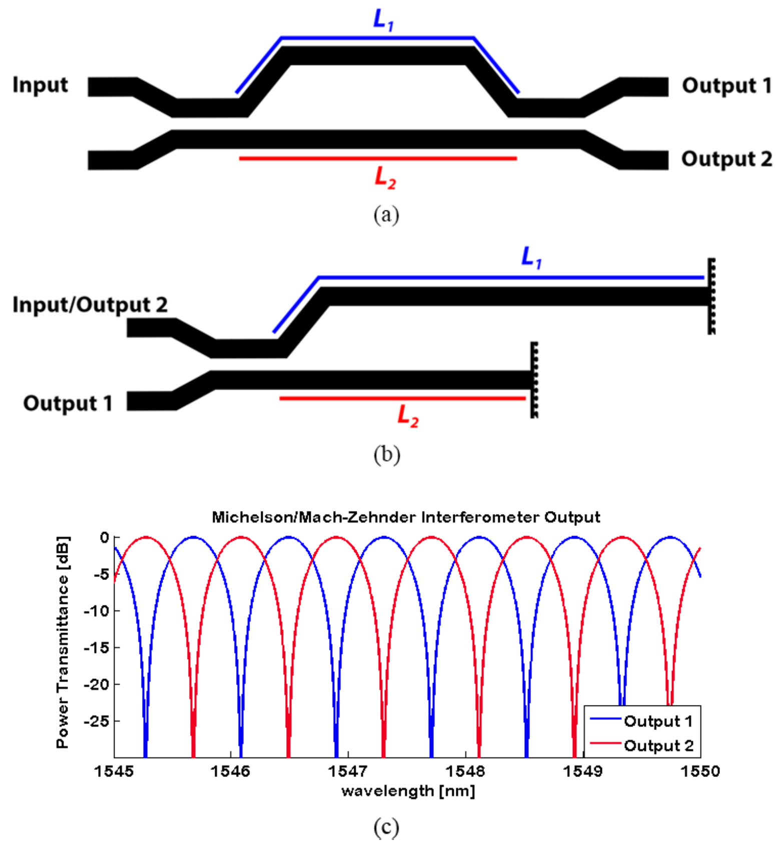


Figure 4-2: Schematic of a planar, directional coupler-based, (a) Mach-Zehnder interferometer and (b) Michelson interferometer with inputs and outputs labelled for de-interleaving applications. (c) 50-to-100 GHz MZI/MI de-interleaver output.

to create a lattice filter with box-like passbands [58]. Figure 4-3 shows how when (a) one, (b) two, and (c) three MZIs are cascaded, the filter spectrum becomes more box-like. While the lattice filter configuration offers design flexibility and has found use in fiber-based applications, many MZIs have to be cascaded in order to get good box-like performance and the devices may become large

One example of a high-performance interleaver in SOI uses ring-resonators coupled to an MZI as shown in Figure 4-4 (a) [59]. Ring-resonators are optical cavities, which, like GTIs, have a periodic response due to a nonlinear phase-shift with an FSR that changes with the time it takes the light to travel around the ring. When ring-resonators are coupled to the arm(s) of a MZI, with proper design, flat passbands are possible. The design was first reported in 1988 by K. Oka *et. al.* [60]. Unlike GTIs, which have

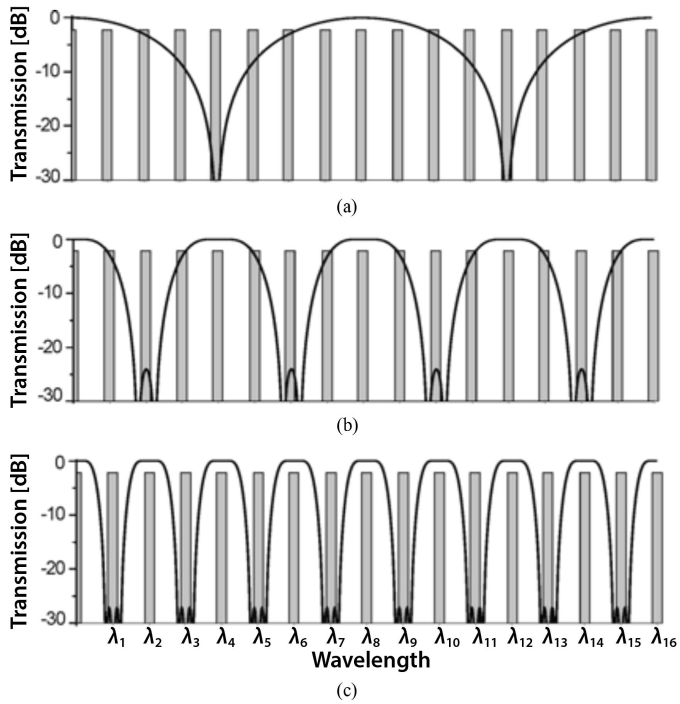


Figure 4-3: MZI lattice filter optical interleaver with (a) one, (b) two, and (c) three cascaded MZIs [57].

resonances based on standing waves, ring-resonators use travelling waves. In ring-assisted MZIs, the strong resonance peaks from the ring-resonator(s) in an all-pass configuration are used to compensate the phase change from the MZI path-length difference response, effectively flattening the passbands and widening the stopbands [57].

Figure 4-4 (b) shows how the 20 dB bandwidth becomes closer to the 3 dB bandwidth, which in an ideal, completely-rectangular, case would be half of the FSR. The reconfigurable triple-ring assisted MZI interleaver with 120 GHz channel spacing is reported to have 20 dB extinction between channels, which prevents channel crosstalk, and box-like passbands across the telecom C-band with a 20 dB bandwidth of 142 GHz [59]. While the footprint of triple ring-assisted MZI is only 0.36 $mm^2$, the ring radius, and thereby, footprint would be increased for narrower channel spacings, such as the ones used in our devices.

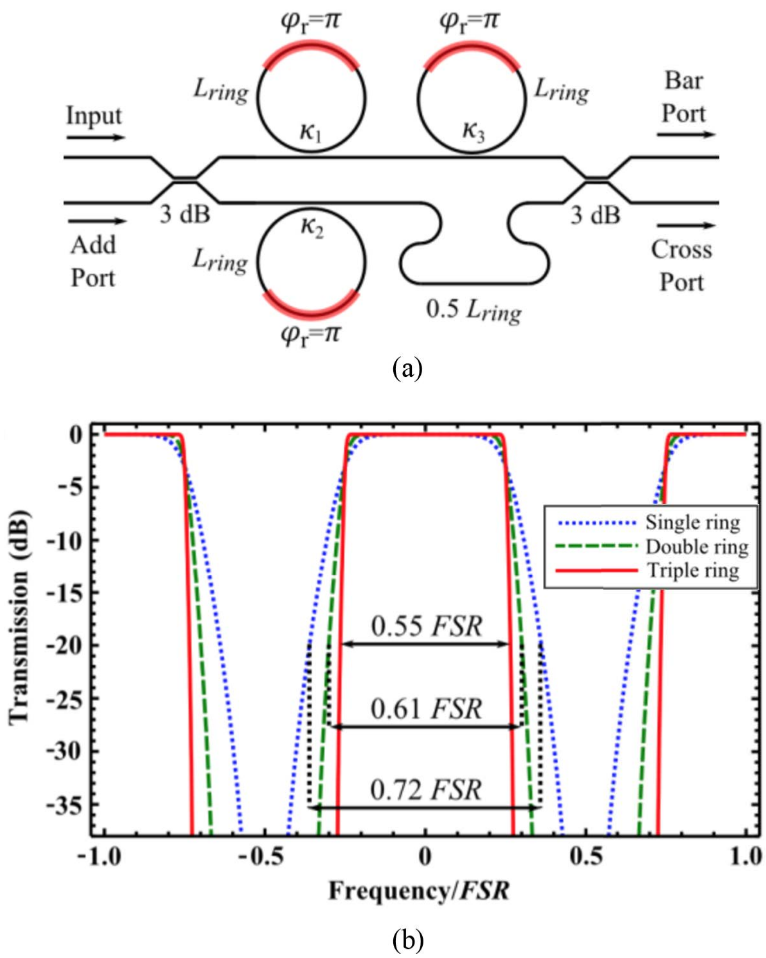


Figure 4-4: (a) Triple ring-assisted MZI interleaver schematic and (b) simulated interleaver spectra for one, two, or three rings coupled to the MZI; as more rings are added, the passbands become box-like with proper selection of parameters [59].

## 4.2 MGTI Design

In the ring-assisted MZI interleaver, narrow channel spacing requires a large ring radius and cascading multiple MZIs takes up chip area. Reflection based interleavers, like the Michelson interferometer, can be more compact in size. One such interleaver design is the MGTI, in which GTIs replace the mirrors of a Michelson interferometer, as shown below in Figure 4-5 for (a) bulk and (b) fibre configurations [55, 61]. While the bulk-optic configuration is not bandwidth limited, the fibre-optic MGTI can only function over the wavelengths in the FBG passbands, as such, chirped fiber Bragg gratings (CFBGs) are chosen in order to increase the grating bandwidth. In the fibre-based configuration shown in Figure 4-5 (b), one mirror of the MI is a CFBG and the other is a distributed Gires-Tournois etalon (DGTE) made by blazing two overlapping CFBGs —one with low reflectance and one with a higher reflectance, forming a superimposed GTI cavity [62]. The transmission spectrum of these devices are shown below in Figure 4-5 (c) and (d) for bulk and fibre-optic configurations, respectively [55, 61].

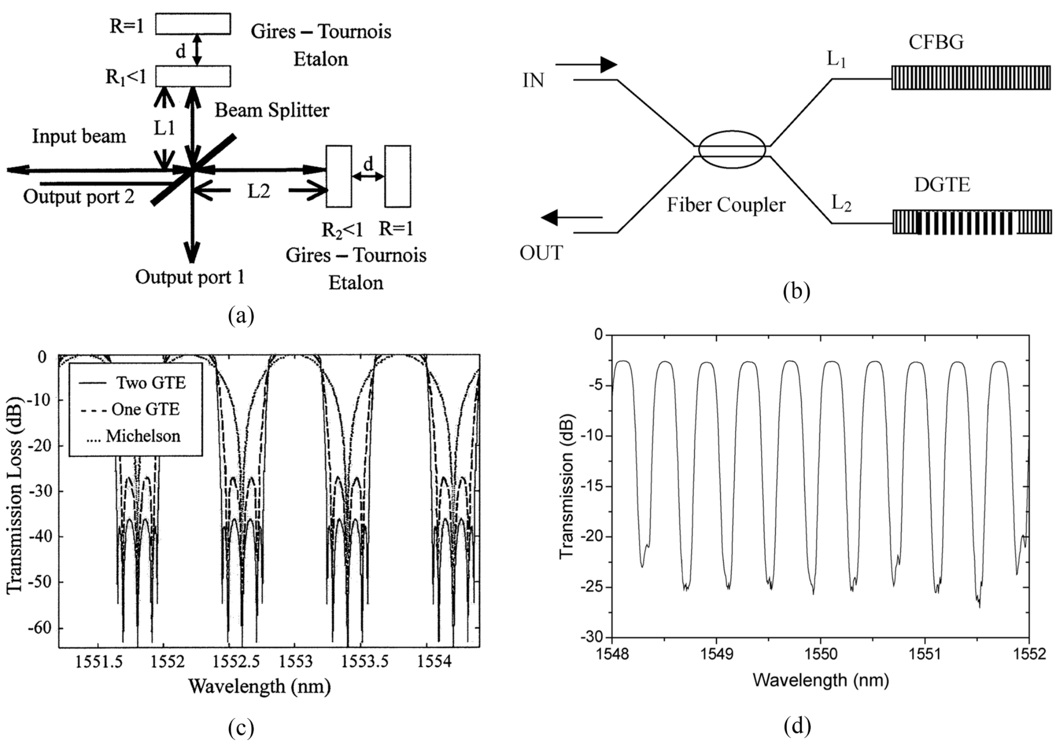


Figure 4-5: Michelson-Gires-Tournois interferometers in (a) bulk- and (b) fibre-optic configurations; measured transmission spectra of (c) bulk- and (d) fibre-optic MGTIs [55, 61].

When no GTI mirrors are used, the interleaver is a Michelson interferometer; upon exchanging one mirror for a GTI, the output spectrum becomes much more box-like; when both mirrors are replaced by GTIs, the extinction ratio and box-like profile is further improved. The output intensity of an MGTI with two GTI mirrors is given by equation 4.2; the sign of ($\pm$) is opposite for port 1 and 2 and perfect 3 dB coupling is assumed:

$$\mathsf{T} = 0.25 \cdot \left[ |\mathsf{r}_{\mathrm{GTI}_1}|^2 + |\mathsf{r}_{\mathrm{GTI}_2}|^2 \pm 2|\mathsf{r}_{\mathrm{GTI}_1}||\mathsf{r}_{\mathrm{GTI}_2}| \cos\left(2\beta\Delta\mathsf{L} + \varphi_{\mathrm{GTI}_1} - \varphi_{\mathrm{GTI}_2}\right) \right] \tag{4.2}$$

where $|\mathsf{r}_{\mathrm{GTI}_1}|$ and $|\mathsf{r}_{\mathrm{GTI}_2}|$ are the reflection coefficient amplitudes of the first and second GTI mirrors, $\varphi_{\mathrm{GTI}_1}$ and $\varphi_{\mathrm{GTI}_2}$ are the phases of the two GTIs, $\Delta\mathsf{L}$ is the path-length difference between the two interferometer arms, $\mathsf{L}_1$ and $\mathsf{L}_2$, and $\beta$ is the propagation constant of the medium. In order for the MGTI to function as an interleaver, $\Delta\mathsf{L}$ must be chosen such that the FSR of the Michelson interferometer (MI) is twice that of the GTIs plus a phase bias of $\pi/2$.

Recently, an MGTI-based interleaver was demonstrated in SOI using cascaded loop mirrors to form the GTI cavities [63]. By utilizing a reflection-based interleaver, the loop-mirror based MGTI in SOI has a smaller footprint than MZI-based interleavers. We use a similar design, but employ waveguide Bragg gratings for the reflective surfaces. In this chapter we demonstrate MGTIs in SOI that are made by using the GTIs detailed in section 3.2. By using the sidewall and offset Bragg gratings to make the GTIs, we are able to tune the reflectance accordingly to optimize the MGTI design. Furthermore, non-uniform grating profiles are possible, which offer an additional level of design flexibility in future devices [32]. A schematic of a sidewall Bragg grating-based MGTI interleaver is shown in Figure 4-6 (a) with the design parameters labeled. It is also possible to make an MGTI interleaver with only one GTI cavity, as shown in Figure 4-6 (b). VGCs are used to couple light to and from the chip and an MMI coupler is used to split the light 50/50 for the Michelson interferometer. The devices are compact; the design in Figure 4-6 (a) has a footprint of $0.4 \times 1.56$ mm.

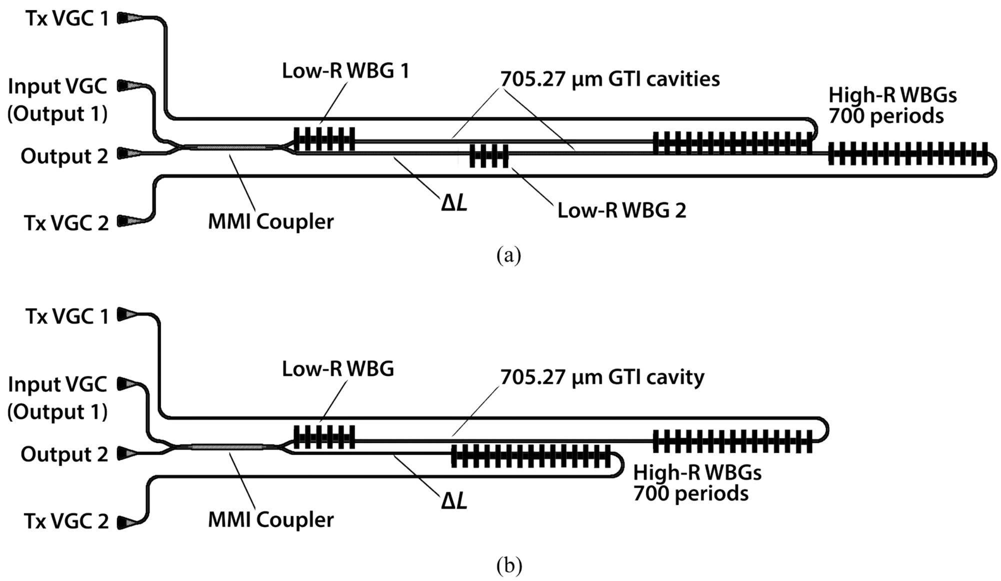


Figure 4-6: Schematic of 50-to-100 GHz sidewall grating-based MGTI interleaver with (a) two GTI cavities and with (b) one GTI cavity.

## 4.3 Grating-Based MGTI Simulations

Once the complex reflection coefficients are calculated for two GTIs using equation 3.2 and the transfer matrix method, they are used in equation 4.2 to determine the relative output intensity of the MGTI interleaver. In order to function as a 50-to-100 GHz interleaver, a path-length difference of 325.713 μm and GTI cavity lengths of 705.276 μm are used. Based on simulation results, 29 and 7 front-grating periods are used in order to have 50.5% and 5.5% reflectance front gratings. Results for a 50-to-100 GHz interleaver are shown in Figure 4-7 (a). The useable filter bandwidth is 16.5 nm, which corresponds to ~41 channels with 50 GHz spacing; an extinction ratio of ~30 dB is simulated. It is also possible to simulate a 100-to-200 GHz interleaver, if a path-length difference of 176.395 μm and GTI cavity lengths of 352.634 μm are used, as shown in Figure 4-7 (b).

A similar extinction ratio and useable filter bandwidth as the 50-to-100 GHz interleaver is observed for the 100-to-200 GHz interleaver, meaning ~21 channels with 100 GHz spacing are simulated; the 3 dB bandwidth is 0.7686 nm and the 20 dB bandwidth is 0.8946 nm, making the simulated 3-to-20 dB bandwidth ratio 1:1.164, which

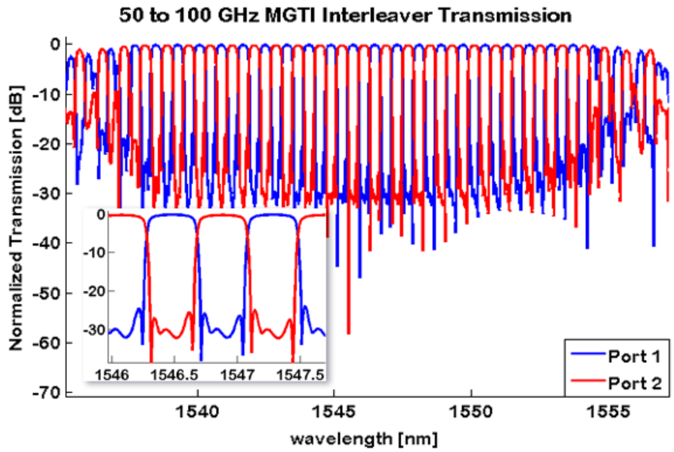


(a)

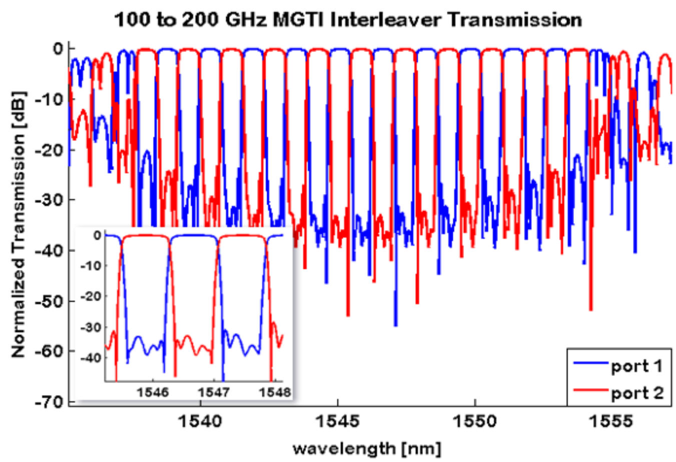


(b)

Figure 4-7: (a) Simulated 50-to-100 GHz MGTI interleaver transmission spectrum for a device with $\Delta L = 352.703\mu m$, $\Lambda = 320.5$ nm, 20 nm corrugation depth, and $d_{GTI} = 705.267\mu m$; (b) Simulated 100-to-200 GHz MGTI interleaver transmission spectrum for a device with $\Delta L = 176.395\mu m$, $\Lambda = 320.5$ nm, 20 nm corrugation depth, and $d_{GTI} = 352.634\mu m$

is less than the reported simulated bandwidth ratio of 1:1.23 for the loop-mirror based MGTI [63]. In equation 4.2, the MGTI output is sensitive to the grating reflectances and the path-lengths of the GTI cavities and Michelson interferometer. Figure 4-8 explores what happens to the simulated spectrum shown in Figure 4-8 (a) when the front-grating reflectances are over or under the optimal 50.5% and 5.5%, when one GTI cavity length is made slightly longer than the other, when the interferometer path-length difference is away from the optimum value, and when the propagation loss is changed.

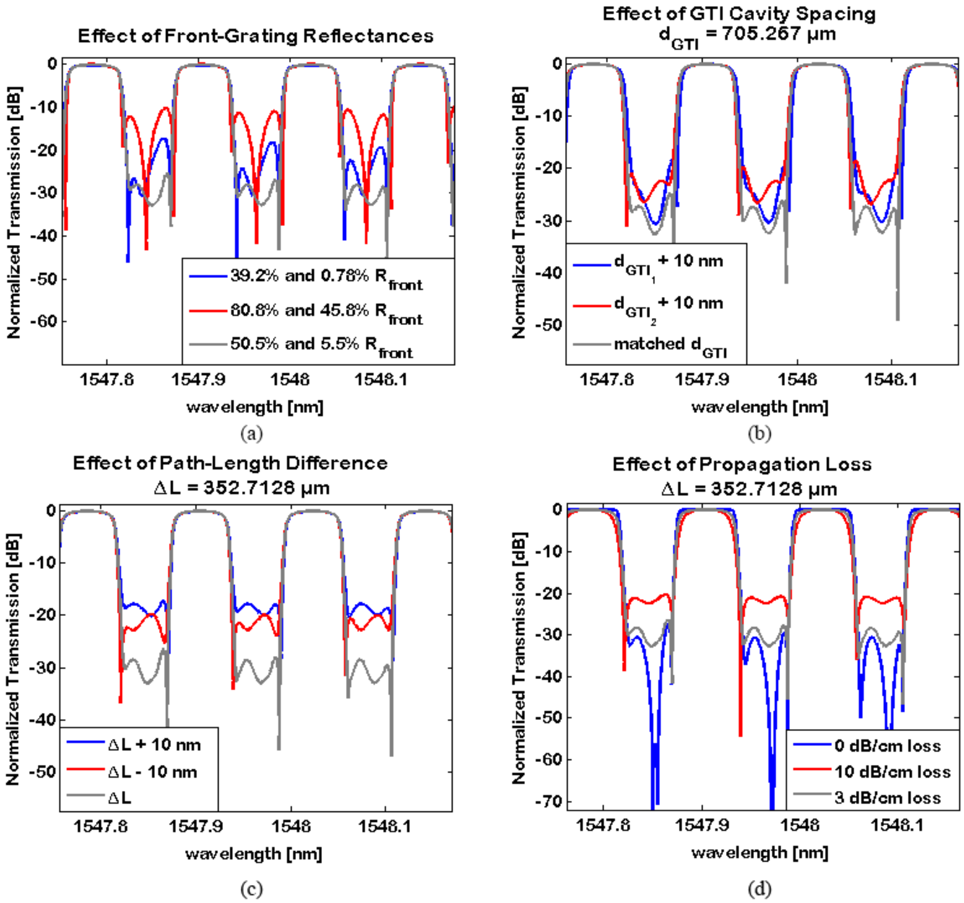


Figure 4-8: Simulated MGTI transmission spectra showing performance degradations from varying design parameters from the optimal values (shown in grey); in (a), the reflectance of the front-gratings are adjusted; (b) one GTI cavity is extended by 10 nm; (c) the interferometer path-length difference is detuned by ± 10 nm; (d) the effect of waveguide propagation loss is investigated

In Figure 4-8 (a) when the grating reflectances are not properly selected, lobes appear in the stopbands, reducing the extinction ratio. When one GTI cavity is made longer than the other, the extinction ratio is reduced, as shown in Figure 4-8 (b). If the interferometer path-length difference is detuned from 352.7128 μm, as in Figure 4-8 (c), the extinction ratio is reduced significantly. The path length values are given with a high level of precision due to the sensitivity in this parameter —if the path-length difference is off by only 0.1%, (i.e. $\Delta L = 353.0665 \mu m$), then the extinction ratio is reduced from ~30 dB to ~10 dB. As in the previous simulations, a propagation loss of 3 dB/cm is assumed. Figure 4-8 (d) shows that for simulated MGTI spectra, if it is assumed to be lossless, the passbands become more box-like, and when the propagation loss is increased from 3 dB/cm to 10 dB/cm, the passbands become more rounded and the extinction ratio is reduced to ~20 dB.

When identical GTIs are measured, the FSR may be consistent, but the specific wavelengths of the resonance peaks can vary on the order of tens or hundreds of picometers, as shown in the measured spectra of two identical GTI structures with 70 front-grating periods, 700 back grating periods, 20 nm corrugation depth, a period of 321.5 nm, and a cavity spacing of 705.267 μm in Figure 4-9 (a); a spectral shift of ~0.05 nm is observed between the two identical devices.

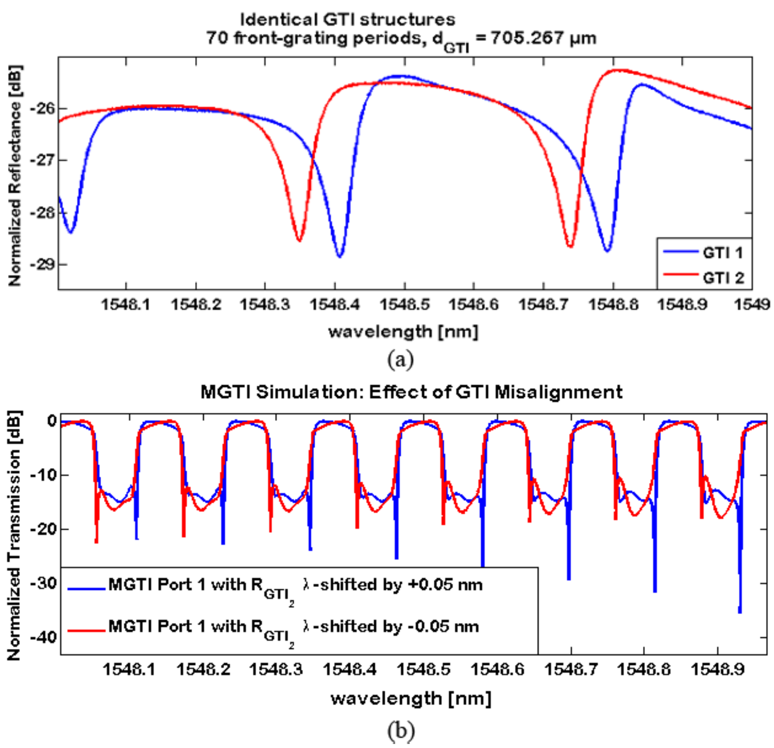


Figure 4-9: Simulated MGTI transmission spectra showing performance degradations from varying design parameters from the optimal values (shown in grey); in (a), the reflectance of the front-gratings are adjusted; (b) one GTI cavity is extended by 10 nm; (c) the interferometer path-length difference is detuned by ± 10 nm; (d) the effect of waveguide propagation loss is investigated

If the GTI are not properly aligned in phase between the two interferometer arms, the interleaver performance is degraded, as shown through simulations in Figure 4-9 (b), in which the MGTI simulation has the same parameters as the one shown in Figure 4-7, except with the reflection coefficient of $GTI_2$ being offset by 0.05 nm in wavelength. As shown in Figure 4-9 (b), a wavelength offset of only 0.05 nm between the GTI spectra degrades the extinction ratio by ~15 dB. In order to help satisfy the phase requirements of equation 4.2, thermal tuning could be used in future designs placing heaters, as in [63], on the GTI cavity lengths and one interferometer arm to control the path-length difference.

## 4.4 Michelson-Gires-Tournois Interferometer Measurement Results

50-to-100 GHz and 100-to-200 GHz MGTI interleaver devices using both short gratings and sidewall offset gratings were fabricated by electron beam lithography on the same chip as the GTIs detailed in section 3.4. In addition, MGTIs were fabricated with one GTI cavity and one grating, as shown in Figure 4-6 (b). Measurement was performed using the same setup shown in Figure 3-10, with the laser input on the "Input VGC" and the output is from "Output 1", as labeled in Figure 4-6. The results of four different grating-based MGTI designs are shown in Figure 4-10. The VGC response in Figure 3-11 is subtracted from the measured spectra to normalize the data.

Figure 4-10 shows the transmission spectra for four different grating-based MGTI designs. When compared to the simulated MGTI responses in Figure 4-7, the biggest difference is observed in the amount of channels that show the expected box-like characteristics; the best response is seen in the six channels nearest to the Bragg-wavelength. When looking at the measured results from the GTIs shown in Figures 3-13 and 3-14, a similar trend is observed, so it makes sense that MGTIs, which are made up of these GTIs, also have a small number of channels. The MGTI bandwidth is limited by the bandwidth of the back-gratings (~7 nm bandwidth for 700 periods). Unlike the simulations, which show an extinction ratio of ~30 dB, the measured devices have only have a few dB of extinction in the stopbands, even on those close to the Bragg wavelength. Looking at equation 4.2, this is likely due to three factors: the reflectances of the front-gratings are not ideal (70 periods and not 100 periods); the resonance peaks, and thereby the phases, of the GTIs are not properly aligned due to fabrication inconsistencies; and the path-length difference in the interferometer arms is not properly selected due to differences between the simulated and actual effective indices.

In Figure 4-10 (b), while not optimized, the MGTI response based on sidewall-shifted gratings shows similar characteristics as Figure 4-10 (a), meaning both grating configurations could be used in future devices as means to control the grating strength. Future designs using a deeper corrugation depth with less periods or more sidewall-shift could potentially increase the grating bandwidth and still achieve the desired reflectances. Figure 4-10 (c) shows the design can be easily extended to accommodate different channel spacings, such as 100 GHz, which could be used in 100-to-200 GHz channel interleaving applications. Although future design optimization could improve the MGTI spectra, the phase terms in equation 4.2 are highly sensitive to fabrication tolerances and like the GTIs, measurements of identical MGTI devices show different performance.

It is interesting to note that the best MGTI response is observed in Figure 4-10 (d), for an MGTI with only one GTI cavity (with 70 front-grating periods), as shown in Figure 4-6 (b). The MGTI spectrum is also well-matched to simulations from TMM, as shown in Figure 4-11. This design is more consistent between identical devices, shows a much more box-like spectra, with flat passbands, and has an extinction ratio of ~15 dB near the Bragg wavelength. The increased performance of the single-GTI MGTI is due to the relaxed phase alignment tolerances when only one GTI is considered. In Figure 4-11, the extinction ratio of the simulated transmission changes when the path-length difference is changed. Due to the sensitivity of the path length difference seen between Figure 4-11 (a) and (b) and fabrication inconsistencies, it is expected that the simulated

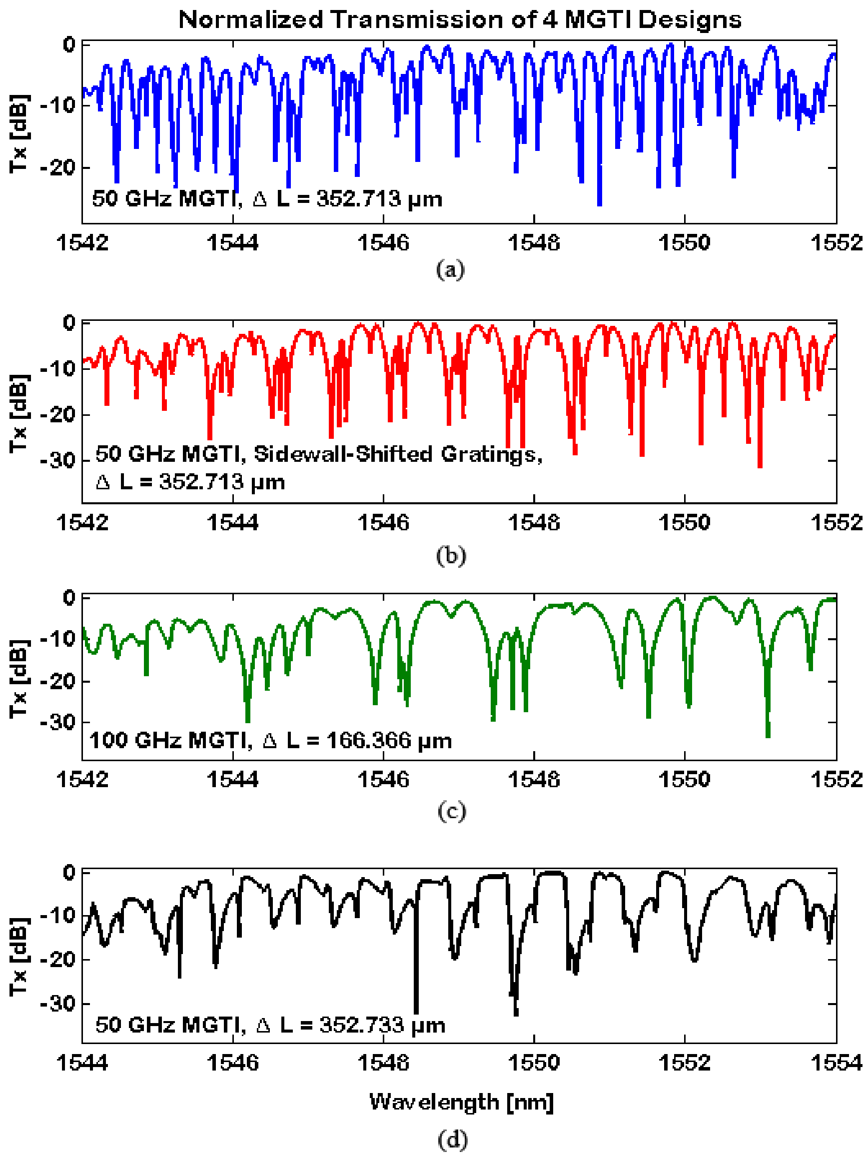


Figure 4-10: Measured reflectance of four different grating-based MGTI designs all with 20 nm corrugation depth and 700 back-grating periods: (a) 50-to-100 GHz interleaver, 20 and 70 front-grating periods, 320.5 nm grating period, GTI cavity length of 705.267 μm, and a path-length difference of 352.713 μm; (b) 50-to-100 GHz interleaver, 100 front-grating periods with shift parameters of 15/20 and 3/20, 321.5 nm grating period, GTI cavity length of 705.267 μm, and a path-length difference of 352.713 μm; (c) 100-to-200 GHz interleaver, 20 and 70 front-grating periods, 321.5 nm grating period, GTI cavity length of 352.634 μm, and a path-length difference of 176.366 μm; and (d) 50-to-100 GHz interleaver, no front-grating on one arm and 70 front-grating periods on the other, 321.5 nm grating period, GTI cavity length of 705.267 μm on both arms, and a path-length difference of 352.7328 μm.

optimal path-length difference will be different than the measured ones. The path-length differences of 352.7027 µm and 352.7327 µm were selected for the MGTI with only one GTI cavity; both path lengths show a box-like spectrum that is well matched to the simulation results near the Bragg wavelength of 1549 nm.

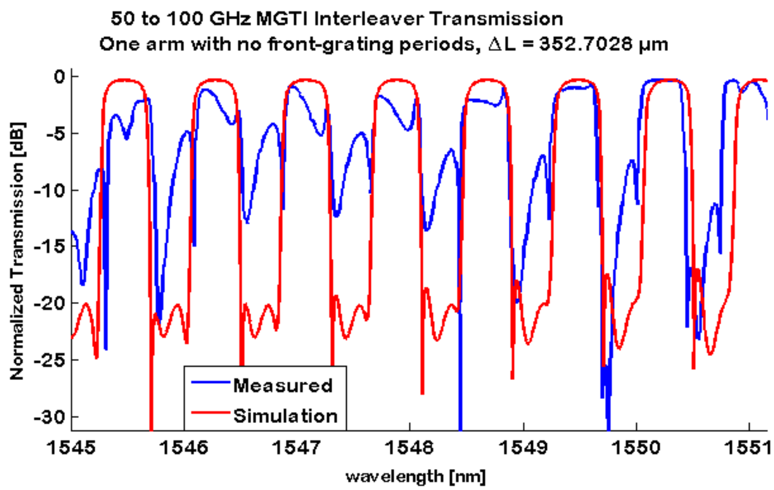


(a)

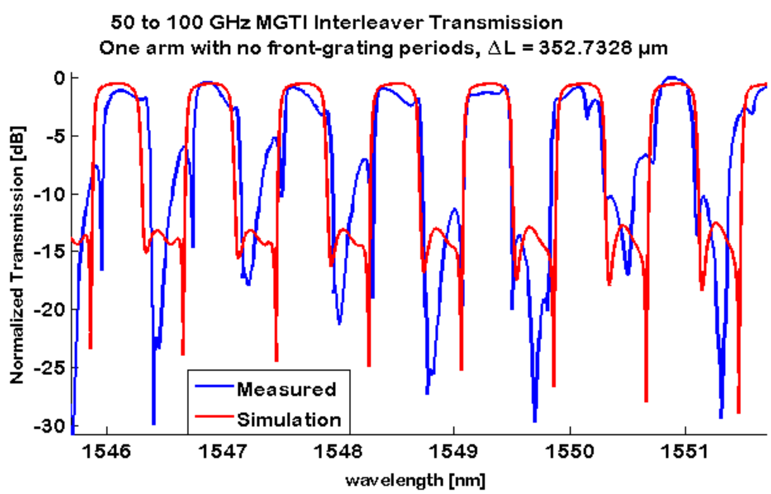


(b)

Figure 4-11: Measured interleaver transmission from (a) an MGTI with one GTI with 70 front-grating periods and another GTI with no front-grating periods, $\Delta L = 352.7028\mu m$, $d_{GTI} = 705.267\mu m$, 20 nm corrugation depth, and a period of 321.5 nm; (b) an MGTI with one GTI with 70 front-grating periods and another GTI with no front-grating periods, $\Delta L = 352.7328\mu m$, $d_{GTI} = 705.267\mu m$, 20 nm corrugation depth, and a period of 321.5 nm; simulated results are for MGTIs with front-grating reflectances of 5.5% and 50.5% —all other parameters are the same as those measured.

## 4.5 Conclusion

The MGTI is a compact configuration for an on-chip optical interleaver and can be made by replacing the mirrors of a Michelson-interferometer with our grating-based GTIs. If properly configured, MGTIs have channel-interleaved output spectra with box-like passbands, offering superior performance to a simple MZI or MI interleaver. By using the complex reflection coefficients of the GTI, determined by the transfer-matrix method results for the Bragg gratings, the spectral response of a sidewall Bragg grating based MGTI is simulated and shows box-like passbands and an extinction ratio of ~30 dB; however, the performance of the MGTI is sensitive to a number of parameters.

In this chapter we demonstrated preliminary results on integrating our GTIs into a Michelson interferometer to make grating-based MGTI interleavers. Four different configurations for grating-based MGTIs were fabricated and measured. MGTI measurement results show some of the desired characteristics, but extinction ratios of only a few dB. Results could be improved with selecting parameters closer to the optimal simulated values, but fabrication inconsistencies between identical devices might make this difficult. Due to the multiple phase terms that need to be properly tuned, it is recommended that future devices be made with thermal heaters on the GTI cavity waveguides and the MGTI path-length difference; the devices with varying grating strengths could then be measured and optimized. We demonstrate it is possible to use short-length or sidewall-shifted gratings for the front-gratings in the MGTIs, but the reflectances have yet to be fully optimized. The channel-spacing can be adjusted by changing the GTI cavity lengths and path-length difference appropriately; we demonstrate both 50-to-100 GHz and 100-to-200 GHz interleavers, however due to measured grating bandwidth of 7 nm for a 700 period grating, the device bandwidth is limited. It is recommended to investigate strategies to have wideband reflectance on the back-gratings, such chirped gratings or loop-mirrors.

The best results are from the MGTI interleaver with only one GTI mirror. While previously reported results of bulk-optic MGTI interleavers show superior performance in an MGTI configuration with two GTI mirrors, our results show that without being able to tune the phases of the two GTIs, the design is not robust enough to take advantage of the two GTIs −however with further optimization of reflectance and phase parameters, perhaps a better MGTI of this configuration could be realized. With the single-GTI MGTI, extinction ratios up to 15 dB are measured and a box-like profile is observed in the pass-bands of the interleaver near the Bragg wavelength. It is recommended that this design be investigated further because of its inherent robustness due to the fact that the phase of only one GTI needs to be controlled. While our MGTIs have yet to be optimized and the phases controlled by thermal tuning, the results clearly show it is possible to use our grating-based GTIs are key components in MGTI interleavers.

# Chapter 5

# Conclusions and Future Work

This thesis presented GTIs made from sidewall-corrugated Bragg gratings in SOI waveguides. Preliminary results for MGTI interleavers built using our GTIs were also presented.

Chapter 2 provided background on silicon photonics, fabrication, and the SOI platform, as well as the building blocks of silicon photonic components used in our devices and photonic circuits: waveguides, waveguide couplers, and vertical grating couplers. Bragg gratings were also introduced and simulation using the transfer matrix method was discussed. Finally, Bragg gratings with offset sidewall corrugations to control the coupling coefficient were introduced as an alternative method of controlling grating reflectance.

Chapter 3 introduced the GTI and its previous implementations in bulk, fibre, and integrated optics. The background on design, fabrication, and the experimental setup for measuring our GTIs was discussed. Simulation results of GTIs based on waveguide Bragg gratings were presented and compared with measurement results of GTIs with varying front-grating reflectance —from both short gratings and sidewall-shifted gratings. It was observed that when the number of periods was reduced or the amount of sidewall-shift was increased, the finesse and extinction ratio was reduced. When the amount of periods in the front-grating of the GTI test structures is reduced to zero, or offset to completely destructively interfere, a cavity response is still observed and is believed to be from reflections off the Y-branch of the GTI test structures. Future work with the GTIs includes investigating how to achieve GTIs with low extinction ratios, such as the ones with ~5.5% reflectance used in MGTI interleavers. Furthermore, the number of channels the GTI is able to filter should be improved in future design by using reflectors with a wider bandwidth. Grating bandwidth could be improved with deeper gratings and less periods or more sidewall-offset; chirped gratings could also be investigated. It is also recommended that future work investigate the phase response of the GTIs for potential on-chip dispersion management applications. As shown in the results presented in this thesis, we conclude it is possible to control the extinction ratio (through the finesse) by either reducing the number of grating periods in the front-grating of the GTI or by offsetting one of the front-grating sidewall −the control over the reflectances is critical when the GTIs are used in Michelson-Gires-Tournois interferometers.

Chapter 4 introduced optical interleavers and some Mach-Zehnder and Michelson interferometer-based configurations in SOI. Background was provided on the MGTI and its previous implementations in bulk, fibre, and integrated optics. Our interleaver design is an MGTI that uses the GTIs from chapter 3 in a Michelson interferometer −a simple silicon photonic circuit. Simulation results of grating-based MGTIs and the effect of detuning various parameters from optimal values were investigated. Preliminary measurement results of four different configurations of MGTI interleavers based on our GTIs were presented, of which the most promising results came from MGTIs with only one GTI mirror, most likely due to the challenges in matching the phases of two GTIs appropriately. For future work, it is recommended that the single-GTI MGTI design be further investigated due to its inherent robustness and optimized to the proper grating reflectances. It is also recommended to use thermal heaters on the Michelson interferometer path-length difference and on the GTI cavity waveguides in order to control and optimize the phases in the MGTI. In order to increase the number of channels, the back grating could be replaced by a loop-mirror or by a chirped grating. Based on the MGTI results shown in chapter 4, it is concluded that it is possible to make an MGTI interleaver based on sidewall-corrugated Bragg gratings and sidewall-shifted gratings.

# Bibliography


[1] D. A. B. Miller, "Device requirements for optical interconnects to silicon chips," *Proceedings of the IEEE*, vol. 97, no. 7, pp. 1166–1185.

[2] S. E. Miller, "Integrated optics: An introduction," *Bell System Technical Journal*, vol. 48, no. 7, pp. 2059–2069.

[3] R. A. Soref, "Silicon-based optoelectronics," *Proceedings of the IEEE*, vol. 81, no. 12, pp. 1687–1706.

[4] S. Fathpour, "Emerging heterogeneous integrated photonic platforms on silicon," *Nanophotonics*, vol. 4, no. 1, 2015.

[5] S. Rumley, D. Nikolova, R. Hendry, Q. Li, D. Calhoun, and K. Bergman, "Silicon photonics for exascale systems," *Lightwave Technology, Journal of*, vol. 33, no. 3, pp. 547–562.

[6] N. Bar-Chaim, K. Y. Lau, I. Ury, and A. Yariv, "Monolithic optoelectronic integration of a gaalas laser, a field-effect transistor, and a photodiode," *Applied Physics Letters*, vol. 44, no. 10, pp. 941–943.

[7] H. Takeuchi and K. Oe, "Low-loss single-mode gaas-algaas miniature optical waveguides with straight and bending structures," *Lightwave Technology, Journal of*, vol. 7, no. 7, pp. 1044–1054, 1989.

[8] H. Takeuchi, K. Kasaya, Y. Kondo, H. Yasaka, K. Oe, and Y. Imamura, "Monolithic integrated coherent receiver on inp substrate," *Photonics Technology Letters, IEEE*, vol. 1, no. 11, pp. 398–400.

[9] R. A. Soref and B. R. Bennett, "Electrooptical effects in silicon," *Quantum Electronics, IEEE Journal of*, vol. 23, no. 1, pp. 123–129.

[10] A. Narasimha, B. Analui, L. Yi, T. J. Sleboda, S. Abdalla, E. Balmater, S. Gloeckner, D. Guckenberger, M. Harrison, R. G. M. P. Koumans, D. Kucharski, A. Mekis, S. Mirsaidi, S. Dan, and T. Pinguet, "A fully integrated $4 \times 10$-gb/s dwdm optoelectronic transceiver implemented in a standard 0.13 μm cmos soi technology," *Solid-State Circuits, IEEE Journal of*, vol. 42, no. 12, pp. 2736–2744.

[11] S. Assefa, S. Shank, W. Green, M. Khater, E. Kiewra, C. Reinholm, S. Kamlapurkar, A. Rylyakov, C. Schow, F. Horst, P. Huapu, T. Topuria, P. Rice, D. M.

Gill, J. Rosenberg, T. Barwicz, Y. Min, J. Proesel, J. Hofrichter, B. Offrein, G. Xiaoxiong, W. Haensch, J. Ellis-Monaghan, and Y. Vlasov, "A 90nm cmos integrated nano-photonics technology for 25gbps wdm optical communications applications," in *Electron Devices Meeting (IEDM), 2012 IEEE International*, pp. 33.8.1–33.8.3.

[12] A. E. J. Lim, S. Junfeng, F. Qing, L. Chao, T. Xiaoguang, D. Ning, C. Kok Kiong, R. P. C. Tern, and L. Tsung-Yang, "Review of silicon photonics foundry efforts," *Selected Topics in Quantum Electronics, IEEE Journal of*, vol. 20, no. 4, pp. 405–416.

[13] P. De Dobbelaere, A. Ayazi, Y. Chi, A. Dahl, S. Denton, S. Gloeckner, K.-Y. Hon, S. Hovey, Y. Liang, M. Mack, G. Masini, A. Mekis, M. Peterson, T. Pinguet, J. Schramm, M. Sharp, C. Sohn, K. Stechschulte, P. Sun, G. Vastola, L. Verslegers, and R. Zhou, "Packaging of silicon photonics systems," in *Optical Fiber Communication Conference*, ser. OSA Technical Digest (online). Optical Society of America, p. W3I.2.

[14] G. Denoyer, A. Chen, B. Park, Z. Yuxin, A. Santipo, and R. Russo, "Hybrid silicon photonic circuits and transceiver for 56gb/s nrz 2.2km transmission over single mode fiber," in *Optical Communication (ECOC), 2014 European Conference on*, pp. 1–3.

[15] L. Jon, Z. Xuezhe, E. Chang, I. Shubin, L. Guoliang, L. Ying, Y. Jin, H. Thacker, L. Jin-Hyoung, F. Liu, P. Amberg, K. Raj, J. E. Cunningham, A. V. Krishnamoorthy, and R. Ho, "Design considerations for a 33mw, 12.5 gbps x 8 channel silicon photonic transmitter array," in *Solid-State Circuits Conference (A-SSCC), 2013 IEEE Asian*, pp. 37–40.

[16] L. Cheng, B. Rui, A. Shafik, E. Z. Tabasy, W. Binhao, T. Geng, M. Chao, C. Chin-Hui, P. Zhen, M. Fiorentino, R. G. Beausoleil, P. Chiang, and S. Palermo, "Silicon photonic transceiver circuits with microring resonator bias-based wavelength stabilization in 65 nm cmos," *Solid-State Circuits, IEEE Journal of*, vol. 49, no. 6, pp. 1419–1436.

[17] X. Dan-Xia, J. H. Schmid, G. T. Reed, G. Z. Mashanovich, D. J. Thomson, M. Nedeljkovic, C. Xia, D. Van Thourhout, S. Keyvaninia, and S. K. Selvaraja, "Silicon photonic integration platform: Have we found the sweet spot?" *Selected Topics in Quantum Electronics, IEEE Journal of*, vol. 20, no. 4, pp. 189–205.

[18] F. Kish, M. Reffle, T. Butrie, M. Ziari, P. Evans, S. Corzine, H. S. Tsai, D. Pavinski, J. Zhang, J. Tang, A. Dentai, R. Muthiah, J. Pleumeekers, D. Lambert, M. Missey, V. La, M. Fisher, S. Murthy, R. Salvatore, S. Demars, A. James, J. Rahn, S. Kumar, M. Mitchell, J. Zhang, L. Tiangong, R. Nagarajan, M. Kato, and D. Welch, "500 gb/s and beyond photonic integrated circuit module transmitters and receivers," in *Optical Fiber Communications Conference and Exhibition (OFC), 2014*, pp. 1–3.

[19] V. Axelrad and M. C. Smayling, "16nm with 193nm immersion lithography and double exposure," vol. 7641, pp. 764 109–764 109–6.

[20] H. Nalwa, *Handbook of Nanostructured Materials and Nanotechnology, Five-Volume Set*. Elsevier Science.

[21] T. Ito and S. Okazaki, "Pushing the limits of lithography," *Nature*, vol. 406, no. 6799, pp. 1027–1031.

[22] R. Olshansky and D. B. Keck, "Pulse broadening in graded-index optical fibers," *Applied Optics*, vol. 15, no. 2, pp. 483–491.

[23] J.-M. Liu, *Photonic Devices*. Cambridge University Press, 2005. [Online]. Available: http://dx.doi.org/10.1017/CBO97805116142

[24] H. H. Li, "Refractive index of silicon and germanium and its wavelength and temperature derivatives," *Journal of Physical and Chemical Reference Data*, vol. 9, no. 3, pp. 561–658.

[25] I. H. Malitson, "Interspecimen comparison of the refractive index of fused silica*,†," *Journal of the Optical Society of America*, vol. 55, no. 10, pp. 1205–1209.

[26] E. Dulkeith, F. Xia, L. Schares, W. M. J. Green, and Y. A. Vlasov, "Group index and group velocity dispersion in silicon-on-insulator photonic wires," *Optics Express*, vol. 14, no. 9, pp. 3853–3863.

[27] C. Incorporated, "Corning smf-28 ultra optical fiber product information."

[28] R. J. Bojko, J. Li, L. He, T. Baehr-Jones, M. Hochberg, and Y. Aida, "Electron beam lithography writing strategies for low loss, high confinement silicon optical waveguides," *Journal of Vacuum Science & Technology B*, vol. 29, no. 6, p. 06F309.

[29] Y. A. Vlasov and S. J. McNab, "Losses in single-mode silicon-on-insulator strip waveguides and bends," *Optics Express*, vol. 12, no. 8, pp. 1622–1631.

[30] X. Qiangfei, F. M. Patrick, G. He, and Y. C. Stephen, "Ultrafast and selective reduction of sidewall roughness in silicon waveguides using self-perfection by liquefaction," *Nanotechnology*, vol. 20, no. 34, p. 345302.

[31] Y. Zhang, S. Yang, A. E.-J. Lim, G.-Q. Lo, C. Galland, T. Baehr-Jones, and M. Hochberg, "A compact and low loss y-junction for submicron silicon waveguide," *Optics Express*, vol. 21, no. 1, pp. 1310–1316.

[32] A. D. Simard and S. LaRochelle, "Complex apodized bragg grating filters without circulators in silicon-on-insulator," *Optics Express*, vol. 23, no. 13, pp. 16 662–16 675.

[33] L. B. Soldano and E. C. M. Pennings, "Optical multi-mode interference devices based on self-imaging: principles and applications," *Lightwave Technology, Journal of*, vol. 13, no. 4, pp. 615–627.

[34] C. Kopp, Bernabe, x, S., B. B. Bakir, J. M. Fedeli, R. Orobtchouk, F. Schrank, H. Porte, L. Zimmermann, and T. Tekin, "Silicon photonic circuits: On-cmos integration, fiber optical coupling, and packaging," *Selected Topics in Quantum Electronics, IEEE Journal of*, vol. 17, no. 3, pp. 498–509.

[35] D. Taillaert, C. Harold, P. I. Borel, L. H. Frandsen, R. M. De La Rue, and R. Baets, "A compact two-dimensional grating coupler used as a polarization splitter," *Photonics Technology Letters, IEEE*, vol. 15, no. 9, pp. 1249–1251.

[36] W. Yun, J. Flueckiger, Y. Han, R. Bojko, N. A. F. Jaeger, and L. Chrostowski, "Focusing sub-wavelength grating coupler," in *Photonics Conference (IPC), 2014 IEEE*, pp. 552–553.

[37] A. Othonos, K. Kalli, D. Pureur, and A. Mugnier, *Fibre Bragg Gratings.* Berlin, Heidelberg: Springer Berlin Heidelberg, pp. 189–269.

[38] T. E. Murphy, J. Todd Hastings, and H. I. Smith, "Fabrication and characterization of narrow-band bragg-reflection filters in silicon-on-insulator ridge waveguides," *Lightwave Technology, Journal of*, vol. 19, no. 12, pp. 1938–1942.

[39] R. Loiacono, G. T. Reed, G. Z. Mashanovich, R. Gwilliam, S. J. Henley, Y. Hu, R. Feldesh, and R. Jones, "Laser erasable implanted gratings for integrated silicon photonics," *Optics Express*, vol. 19, no. 11, pp. 10 728–10 734.

[40] K. A. P. P. W. R. L. G. Z. M. G. T. R. Bulk, B.P and R. M. Gwilliam, "Optical filters utilizing ion implanted bragg gratings in soi waveguides," *Advances in Optical Technologies*, vol. 2008.

[41] T. C. Kleckner, D. Modotto, A. Locatelli, J. P. Mondia, S. Linden, R. Morandotti, C. De Angelis, C. R. Stanley, H. M. van Driel, and J. S. Aitchison, "Design, fabrication, and characterization of deep-etched waveguide gratings," *Lightwave Technology, Journal of*, vol. 23, no. 11, pp. 3832–3842.

[42] W. Xu, S. Wei, R. Vafaei, N. A. F. Jaeger, and L. Chrostowski, "Uniform and sampled bragg gratings in soi strip waveguides with sidewall corrugations," *Photonics Technology Letters, IEEE*, vol. 23, no. 5, pp. 290–292.

[43] A. D. Simard and S. LaRochelle, "High performance narrow bandpass filters based on integrated bragg gratings in silicon-on-insulator," in *Optical Fiber Communications Conference and Exhibition (OFC), 2015*, pp. 1–3.

[44] W. Junjia, R. Ashrafi, M. Rochette, and L. R. Chen, "Chirped microwave pulse generation using an integrated sip bragg grating in a sagnac loop," *Photonics Technology Letters, IEEE*, vol. 27, no. 17, pp. 1876–1879.

[45] W. Junjia and L. R. Chen, "Bandpass bragg grating transmission filters and optical add-drop multiplexers on silicon-on-insulator," in *Photonics Conference (IPC), 2014 IEEE*, pp. 56–57.

[46] J. R. Philip St, A. Jean-Luc, and R. Laurence, "Fibre gratings," *Physics World*, vol. 6, no. 10, p. 41.

[47] S. Huang, M. LeBlanc, M. M. Ohn, and R. M. Measures, "Bragg intragrating structural sensing," *Applied Optics*, vol. 34, no. 22, pp. 5003–5009.

[48] X. Wang, Y. Wang, J. Flueckiger, R. Bojko, A. Liu, A. Reid, J. Pond, N. A. F. Jaeger, and L. Chrostowski, "Precise control of the coupling coefficient through destructive interference in silicon waveguide bragg gratings," *Optics Letters*, vol. 39, no. 19, pp. 5519–5522.

[49] F. Gires and P. Tournois, "Interferometre utilisable pour la compression d'impulsions lumineuses modulees en frequence," *Comptes rendus hebdomadaires des séances de l'Académie des sciences*, vol. 258, no. 5, pp. 6112–6115, 1964.

[50] J. Kuhl and J. Heppner, "Compression of femtosecond optical pulses with dielectric multilayer interferometers," *Quantum Electronics, IEEE Journal of*, vol. 22, no. 1, pp. 182–185.

[51] S. Xuewen, K. Sugden, P. Rhead, J. Mitchell, I. Felmeri, G. Lloyd, K. Byron, H. Zhijian, I. Khrushchev, and I. Bennion, "Tunable dispersion compensator based on distributed gires-tournois etalons," *Photonics Technology Letters, IEEE*, vol. 15, no. 8, pp. 1111–1113.

[52] X. Shu, K. Sugden, and K. Byron, "Bragg-grating-based all-fiber distributed gires-tournois etalons," *Optics Letters*, vol. 28, no. 11, pp. 881–883.

[53] R. St-Gelais, T. Kerrien, H. Camirand, A. Poulin, and Y. A. Peter, "Silicon-on-insulator in-plane gires-tournois interferometers," *Photonics Technology Letters, IEEE*, vol. 24, no. 24, pp. 2272–2275.

[54] F. Van Laere, G. Roelkens, M. Ayre, J. Schrauwen, D. Taillaert, D. Van Thourhout, T. F. Krauss, and R. Baets, "Compact and highly efficient grating couplers between optical fiber and nanophotonic waveguides," *Journal of Lightwave Technology*, vol. 25, no. 1, pp. 151–156.

[55] H. Chao-Hsing, R. Wang, Z. J. Wen, I. McMichael, Y. Pochi, L. Chao-Wei, and C. Wood-Hi, "Flat-top interleavers using two gires-tournois etalons as phase-dispersive mirrors in a michelson interferometer," *Photonics Technology Letters, IEEE*, vol. 15, no. 2, pp. 242–244.

[56] ITU-T, "Spectral grids for wdm applications: Dwdm frequency grid," International Telecommunication Union, Recommendation G.694.1.

[57] R. de Ridder and C. H. Roeloffzen, *Interleavers*, ser. Springer Series in Optical Sciences. Springer Berlin Heidelberg, vol. 123, ch. 10, pp. 381–432.

[58] S. Cao, J. Chen, J. N. Damask, C. R. Doerr, L. Guiziou, G. Harvey, Y. Hibino, H. Li, S. Suzuki, K. Y. Wu, and P. Xie, "Interleaver technology: comparisons and applications requirements," *Lightwave Technology, Journal of*, vol. 22, no. 1, pp. 281–289.

[59] L.-W. Luo, S. Ibrahim, A. Nitkowski, Z. Ding, C. B. Poitras, S. J. Ben Yoo, and M. Lipson, "High bandwidth on-chip silicon photonic interleaver," *Optics Express*, vol. 18, no. 22, pp. 23 079–23 087.

[60] K. Oda, N. Takato, H. Toba, and K. Nosu, “A wide-band guided-wave periodic multi/demultiplexer with a ring resonator for optical fdm transmission systems,” *Journal of Lightwave Technology*, vol. 6, no. 6, pp. 1016–1023, 1988.

[61] S. Xuewen, K. Sugden, and I. Bennion, “Novel multipassband optical filter using all-fiber michelson-gires-tournois structure,” *Photonics Technology Letters, IEEE*, vol. 17, no. 2, pp. 384–386.

[62] R. Slavik, S. Doucet, and S. LaRochelle, “High-performance all-fiber fabry-perot filters with superimposed chirped bragg gratings,” *Journal of Lightwave Technology*, vol. 21, no. 4, pp. 1059–1065.

[63] J. Xinhong, J. Wu, Y. Yang, T. Pan, J. Mao, B. Liu, R. Liu, y. zhang, C. Qiu, and Y. Su, “Compact silicon photonic interleaver using loop-mirror-based michelson-gires-tournois interferometer,” in *Optical Fiber Communication Conference*, ser. OSA Technical Digest (online). Optical Society of America, p. Tu2F.5.